WE-NEED

WatEr NEEDs, availability, quality and sustainability

Deliverable Number:	D1.4b
Work package number:	WP1
Deliverable title	REPORT ON CHARACTERIZATION OF FIELD SITES
Type	Report
Dissemination Level	Public
Lead participant	Politecnico di Milano
Contributing scientists and other personnel	Emanuela Bianchi Janetti, Martina Siena, Ceriotti Giulia, Dell'Oca Aronne, Alberto Guadagnini, Giovanni M Porta, Monica Riva
Scheduled delivery date	20/10/2018
Actual / forecast delivery date	20/11/2018

Deliverable summary

This document complements Deliverable 1.4a and provides conclusive results obtained in the context of hydrogeological characterization of the two field sites analyzed in the project: Cremona and Bologna Aquifer systems, located in the Po Plain, Northern Italy. For the Cremona site, we explore the relative influence of parametric uncertainties to steady-state hydraulic head distributions across the set of conceptual models considered by way of a moment-based Global Sensitivity Analysis, GSA, which takes into account the influence of uncertain parameters on multiple (statistical) moments of a given model output. This new methodology has been developed during the project. Due to computational costs, moment-based indices are obtained numerically through the use of a model-order reduction technique based on the polynomial chaos expansion approach. We then use results of GSA to drive calibration of model parameters including the most influential hydraulic conductivity values of the geomaterials composing the aquifer and natural springs leakage coefficient. For the Bologna site, we investigate facies connectivity in a Monte Carlo (MC) framework, by relying on two sets of 100 realizations generated with two diverse geostatistical reconstruction techniques (SISIM and TPROGS). In particular, our goal is to evaluate quantitatively (i) the connectivity of the diverse facies in each individual realization, (ii) the variability of connectivity within a set of equally-likely facies distributions, and (iii) the extent at which the generation method affects facies connectivity. We investigate possible effects of connectivity on groundwater flow and parameter calibration. Finally, we take advantage of model identification criteria and a multi-model approach to compute hydraulic head estimates from all MC realizations.

D1.4b
Report on characterization of field sites

Contents

1. Introduction

This deliverable provides conclusive results obtained in the context of hydrogeological characterization of the two field sites analysed within the project: the Bologna and the Cremona Aquifer systems, representing different but complementary realities. The Bologna Aquifer is a key source of water for the metropolitan area of Bologna. The Cremona Aquifer is located in the so-called Springs Belt. Natural high-quality water springs are the main supply to agriculture and a key environmental driver. The Bologna and Cremona sites are archetypal of two distinct realities of alluvial aquifers, and can be considered representative of diverse environmental settings of Europe-wide interest.

The deliverable is structured as follows: Section 2 provides the analysis performed for the Cremona site. The moment based Global Sensitivity Analysis (GSA) is described in Section 2.1. Section 2.2 focuses on natural spring modelling and model calibration.

Section 3.1 illustrates the results of the investigation of facies connectivity performed on the Bologna site. Section 3.2 describes the groundwater flow model and in Section 3.3 we discuss the effects of connectivity on the calibration of model parameters. In Section 3.4, we apply a multi-model approach to obtain hydraulic head estimates from all MC realizations.

2. Cremona site

The study area is part of the high-medium Alluvial Po Plain. It lies between the city of Bergamo (Northern Italy) and the confluence of the Adda and Serio rivers (see Figure 2.1 of Deliverable 1.4a). A key feature of the study area is the occurrence of high-quality water springs, which are the main supply to agriculture and a key environmental driver.

In Deliverable 1.4a we developed a conceptual and a numerical model of the study area. In particular, on the bases of lithological data, we reconstructed the three dimensional distribution of facies within the aquifer by means of two geostatistical methods: the *Composite medium approach* (*CM*) and the *Overlapping Continuum Approach* (*OC*). Then, we analysed the impact of the uncertainty in (a) the conceptual model (the two variants of *OC* versus *CM*), (b) the boundary conditions and (c) the hydraulic parameters on the groundwater system response, as quantified in terms of steady-state hydraulic heads obtained at a set of 39 target locations, covering the full investigated area. This analysis has been performed by relying on two Global Sensitivity Analysis, GSA, classical methodologies: (a) a derivative-based approach, which rests on the Morris indices (Morris, 1991) and (b) a variance-based approach, based on the evaluation of the Sobol' indices (Sobol, 1993, 2001).

In the present document we further refined the results of Deliverable D1.4a by providing the outcomes of a novel moment-based GSA (Dell'Oca et al., 2017). These results allow to reach a more complete picture of the system response to variation of uncertain model parameters. The new metrics proposed by Dell'Oca et al. (2017), termed AMA indices, allow to quantify the relative contribution of each uncertain model parameter to the main features (as rendered by the statistical moments) of the probability density function of a model output, y.

One of the main findings of Dell'Oca et al. (2017) is that relying on classical variance-based GSA methods, with the implicit assumption that the uncertainty of y is fully characterized by its variance, can lead at best to an incomplete picture of the system response to model parameter uncertainties. In Section 2.2 we focus on model calibration. In particular, we calibrate natural spring leakage coefficient as well as the most influent hydraulic parameter for each conceptualization using available measurements of hydraulic head and springs flow rate.

2.1 Moment-based Global Sensitivity Analysis

We analyze the impact of the uncertainty in the conceptual model (*CM* and two variants of the *OC*, according to which hydraulic conductivity is computed as a weighted arithmetic or geometric mean of the hydraulic conductivity of the five geomaterials composing the domain, see Deliverable 1.4a for details), boundary conditions and hydraulic parameters on the groundwater system response, as quantified in terms of steady-state hydraulic heads obtained at a set of 39 wells, whose locations are depicted in Figure 2.1, covering the full investigated area. At the same locations hydraulic head measurements are available. These latter will be used during model calibration (Section 2.2).

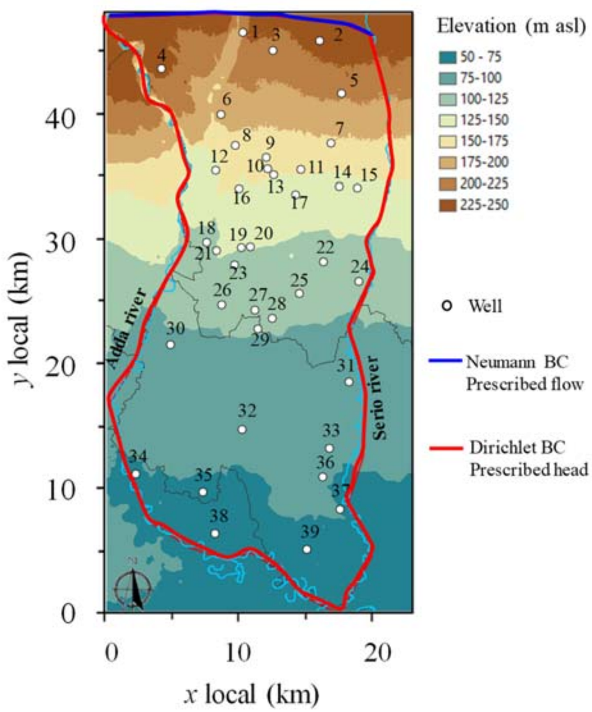

Figure. 2.1. Locations at which GSA metrics are evaluated and boundary conditions of the numerical model.

In order to perform moment-based GSA, as discussed in Deliverable 1.4a, the uncertain model inputs associated with (*a*) hydraulic conductivity values (k_i, with i = 1,…, 5) of the five geomaterials composing the subsurface, (*b*) the total flow rate entering the domain from the Northern boundary, and (*c*) the Dirichlet boundary conditions set along the rivers are collected in a *N*-dimensional vector **p**. Entries of the latter are independent and identically distributed (i.i.d.) random variables, p_i (with i = 1,…, N; N = 7), each characterized by a uniform probability density function, pdf. The (random) parameter space is then defined as $\mathbf{\Gamma} = \left[\mathbf{p}^{\min}, \mathbf{p}^{\max}\right]$ where $\mathbf{p}^{\min}$ and $\mathbf{p}^{\max}$ indicate vectors respectively containing lower ($p_i^{\min}$) and upper ($p_i^{\max}$). The choice of $p_i^{\min}$ and $p_i^{\max}$ (i = 1,…,5) is based on typical hydraulic characteristics of each geomaterial class. With reference to boundary conditions, Rametta (2008) estimated a total incoming flow rate in the area of interest equal to $\overline{p}_6$ = 9.65 m^3/s. Since this estimated value is affected by uncertainty and the spatial distribution of $\overline{p}_6$ is unknown, we consider the incoming flow rate as uniformly distributed along the Northern domain boundary and set $p_6^{\min} = 0.5 \times \overline{p}_6$ and $p_6^{\max} = 1.5 \times \overline{p}_6$ (resulting in a coefficient of variation of about 30%). The support of the Dirichlet boundary condition (p_7) has been defined considering that the river stage may vary between the river bottom and the banks' elevation. A list of selected uncertain parameters and associated range of variability is reported in Table 2.2 of Deliverable 1.4a.

2.1.1 Methodology

The AMA indices (introduced by Dell'Oca et al., 2017) allow quantifying the expected variation of a given statistical moment $M[f]$ of the pdf of $f(\mathbf{p})$. These are defined as

$$\mathrm{AMA}M_{p_i} = \begin{cases} \dfrac{1}{\left|M\left[f\right]\right|} \displaystyle\int_{\Gamma_{p_i}} \left|M\left[f\right] - M[f \mid p_i]\right| \rho_{\Gamma_{p_i}} dp_i & \text{if } M\left[f\right] \neq 0 \\ \displaystyle\int_{\Gamma_{p_i}} \left|M\left[f\right] - M[f \mid p_i]\right| \rho_{\Gamma_{p_i}} dp_i & \text{if } M\left[f\right] = 0 \end{cases} \tag{2.1}$$

$$\mathrm{AMA}M_{p_1,\ldots,p_s} = \begin{cases} \dfrac{1}{\left|M\left[f\right]\right|} \displaystyle\int_{\Gamma_{p_1,\ldots,p_s}} \left|M\left[f\right] - M[f \mid p_1,\ldots,p_s]\right| \rho_{\Gamma_{p_1,\ldots,p_s}} dp_1 \ldots dp_s & \text{if } M\left[f\right] \neq 0 \\ \displaystyle\int_{\Gamma_{p_1,\ldots,xp}} \left|M[f \mid p_1,\ldots,p_s]\right| \rho_{\Gamma_{p_1,\ldots,p_s}} dp_1 \ldots dp_s & \text{if } M\left[f\right] = 0 \end{cases} \tag{2.2}$$

Here, $\mathrm{AMA}M_{p_i}$ (2.1) and $\mathrm{AMA}M_{p_1,\ldots,p_s}$ (2.2) correspond to the AMA indices associated with a given statistical moment M and related to variations of only p_i or considering interactions among $\{p_1,\ldots,p_s\}$, respectively; $\rho_{\Gamma_{p_i}}$ is the marginal pdf of p_i, $\rho_{\Gamma p_1,\ldots,p_s}$ being the joint pdf of $\{p_1,\ldots,p_s\}$; and $M[f \mid p_1,\ldots,p_s]$ indicates conditioning of the (statistical) moment M on known values of parameters $p_1,\ldots,p_s$. Note that $\mathrm{AMA}V_{p_i}$, i.e., the AMA index related to the variance ($M = V$) of $f(\mathbf{p})$, coincides with the principal Sobol' index S_{p_i} only if the conditional variance, $V[f \mid p_i]$ is always (i.e., for each value of p_i) smaller than (or equal to) its unconditional counterpart $V[f]$.

The numerical evaluation of AMA indices can be time consuming and can become unfeasible in complex scenarios, such as the one here considered. These metrics are evaluated relying on a surrogate model based on the generalized Polynomial Chaos Expansion (gPCE) (Ghanem and Spanos, 1991; Xiu and Karniadakis, 2002; Le Maître and Knio, 2010). This technique consists in approximating $f(\mathbf{p})$ by a linear combination of multivariate Legendre polynomials, i.e., $\psi_{\boldsymbol{x}}(\boldsymbol{p})$

$$
\begin{aligned}
&f(\boldsymbol{p}) \cong f_0 + \sum_{i=1}^{N}\sum_{\boldsymbol{x}\in\Im_i}\beta_{\boldsymbol{x}}\psi_{\boldsymbol{x}}(\boldsymbol{p}) + \sum_{i=1}^{N}\sum_{j=1}^{N}\sum_{\boldsymbol{x}\in\Im_{i,j}}\beta_{\boldsymbol{x}}\psi_{\boldsymbol{x}}(\boldsymbol{p}) + \ldots; \\
&\psi_{\boldsymbol{x}}(\boldsymbol{p}) = \prod_{i=1}^{N_p}\psi_{i,x_i}(p_i); \quad \beta_{\boldsymbol{x}} = \int_{\Gamma} f(\boldsymbol{p})\psi_{\boldsymbol{x}}(\boldsymbol{p})\rho_{\Gamma_{\boldsymbol{p}}}\, d\boldsymbol{p},
\end{aligned}
\tag{2.3}
$$

where $\boldsymbol{x} = \{x_1,\ldots,x_N\} \in \mathrm{N}^N$ is a multi-index expressing the degree of each univariate polynomial, $\psi_{i,x_i}(p_i)$; $\beta_{\boldsymbol{x}}$ are the gPCE coefficients; $\rho_{\Gamma_{\boldsymbol{p}}}$ is the pdf of $\mathbf{p}$; $\Im_i$ contains all indices such that only the *i*-th component does not vanish; $\Im_{i,j}$ contains all indices such that only the *i*-th and *j*-th components are not zero, and so on.

2.1.2 Results and discussion

The computational cost linked to the construction of the gPCE depends on the order of truncation, *w*, of the series in (2.3). In this study, we first compare the results obtained up to *w* = 4, requiring 2437 runs of the full flow model. Figure 2.2 depicts (*i*) the AMA indices linked to the mean, $\mathrm{AMA}E_{p_i}$ (Figure 2.2a), variance, $\mathrm{AMA}V_{p_i}$ (Figure 2.2b), and skewness, $\mathrm{AMA}\gamma_{p_i}$ (Figure 2.2c), computed at all 39 target locations for *CM* and considering all seven uncertain model inputs p_i. Note that each well is associated with an Identification Number (ID) which increases from North to South to facilitate the interpretation of the results (see also Figure 2.1). Corresponding results for settings associated with the *OC* modeling strategies (termed as *OC_A* and *OC_G*, when considering the arithmetic or geometric averaging operator, respectively) are depicted in Figures 2.3 and 2.4.

For all conceptual models $\mathrm{AMA}E_{p_i}$ tends to decrease from North to South (see Figures 2.2a, 2.3a and 2.4a). Indices $\mathrm{AMA}E_{p_i}$, quantifying the impact of uncertain inputs on the mean hydraulic heads, are in general very low for *OC_A* and *CM* while they can be significant (> 20%) for *OC_G*. Results obtained with the total Sobol indices $S_{p_i}^T$ (see Deliverable D1.4a) and $\mathrm{AMA}V_{p_i}$ appear to be not always consistent for *CM* model. For example, while the analysis of $S_{p_i}^T$ (See Figure 2.11c of Deliverable 1.4a) would suggest to neglect the impact of k_2, k_4, and p_6 on the variance of model outputs in *CM*, index $\mathrm{AMA}V_{p_i}$ (Figure 2.2b) indicates that the uncertainty of these model inputs can influence the target model output.

In order to grasp the reasons underpinning this finding, we plot in Figure 2.5a-c the conditional variance $V\left[f\middle|p_i\right]$ versus p_i at a selected observation wells (ID 32), together with its unconditional counterpart. Here, the interval of variation of each model parameters has been normalized to span the range [0, 1] for graphical representation purposes. Conditional moments are obtained via 2 × 10^6 runs of the gPCE-based surrogate model.

We note that $V\left[f\middle|k_2\right]$, $V\left[f\middle|k_4\right]$, and $V\left[f\middle|p_6\right]$ for *CM* (Figure 2.5a) can be smaller or higher than their unconditional counterparts, depending on the conditioning value p_i. This behavior explains why the Sobol' sensitivity measure does not allow to completely detect the effect of k_2, k_4, and p_6 on the model output variance at some observation wells. A similar conclusion can be drawn from Figures 2.4c and Figure 2.13c of Deliverable 1.4a, with reference to parameters k_2 and k_4 and model *OC_G*. Conversely, $\mathrm{AMA}V_{p_i}$ and $S_{p_i}^T$ exhibit very consistent features for *OC_A* (Figures 2.3b and Figure 2.12c of Deliverable 1.4a), identifying k_3, k_5, and p_7 as the most influential parameters. Figure 2.5b reveals that $V\left[f\middle|k_5\right]$ and $V\left[f\middle|p_7\right]$ are always smaller than the unconditional variance and, at this well (ID 32), only parameters k_5 and p_7 are influential to the variance of the target output for *OC_A* as shown in Figure 2.3b.

The degree of symmetry of the pdfs of hydraulic heads, as driven by the skewness, strongly depends on the considered conceptual model and on the selected observation well. In most of the observation wells the unconditional pdf is right-skewed for *CM* and *OC_G* while being left-skewed or symmetric for *OC_A* (not shown). As an example, the unconditional and conditional skewness obtained for the three considered models via 2 × 10^6 runs of the gPCE-based surrogate model are depicted in Figure 2.5d-f at observation well (ID 32). Conditioning on model parameters affects the shape of the pdf, whose degree of symmetry can markedly depend on the conditioning value of p_i.

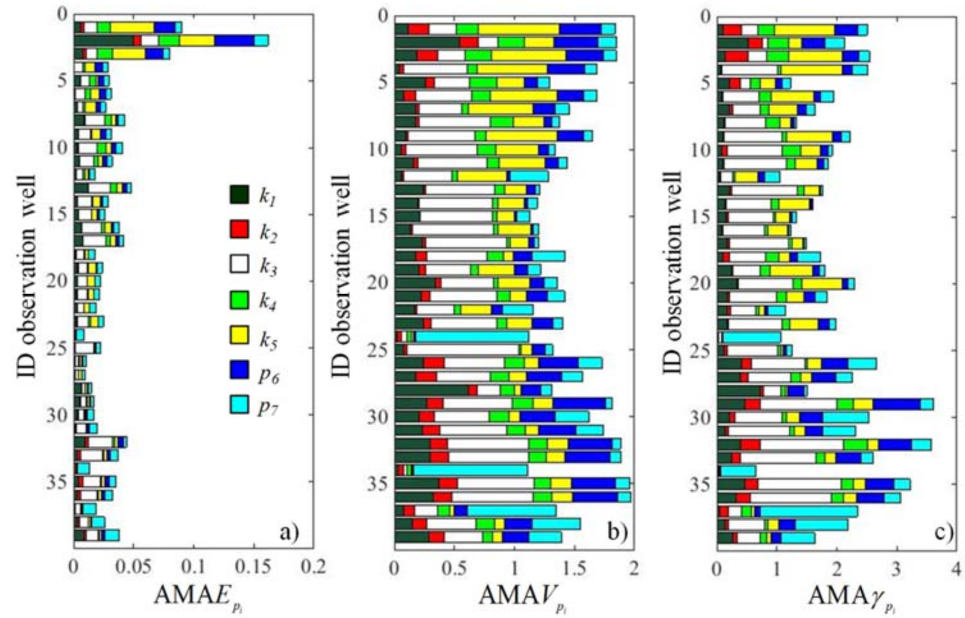

Figure 2.2. *CM* approach. a) $\mathrm{AMA}E_{p_i}$, b) $\mathrm{AMA}V_{p_i}$ and c) $\mathrm{AMA}\gamma_{p_i}$ indices evaluated at the 39 locations depicted in Figure 2.1.

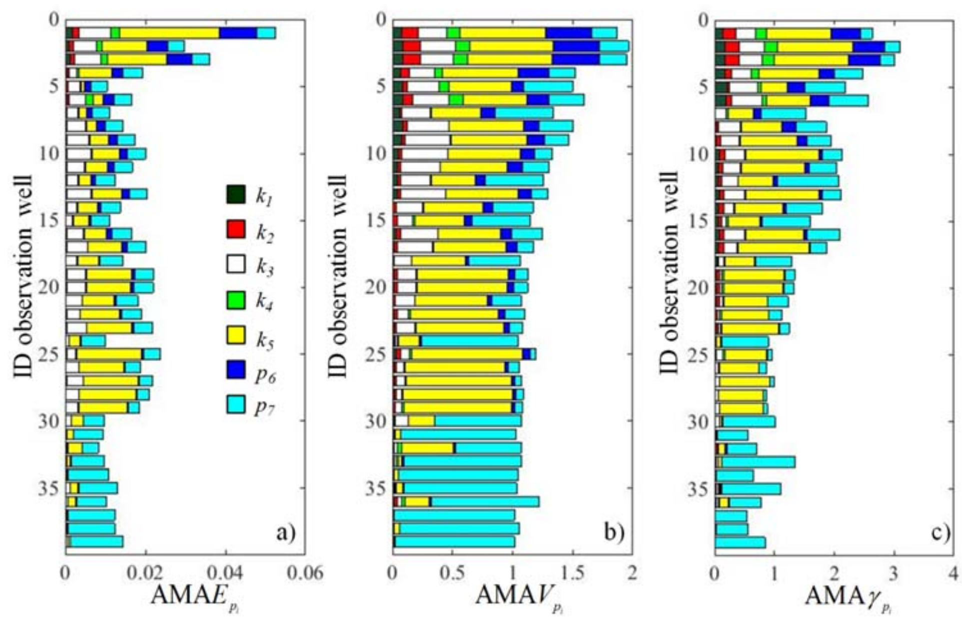

Figure 2.3. *OC_A* approach. a) $\mathrm{AMA}E_{p_i}$, b) $\mathrm{AMA}V_{p_i}$ and c) $\mathrm{AMA}\gamma_{p_i}$ indices evaluated at the 39 locations depicted in Figure 2.1.

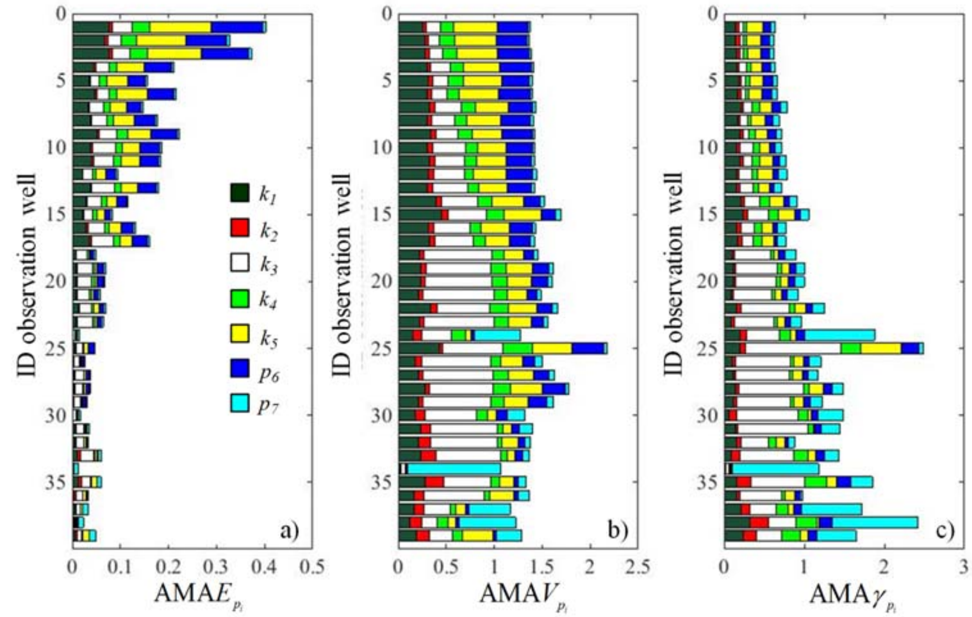

Figure 2.4. *OC_G* approach. a) $\mathrm{AMA}E_{p_i}$, b) $\mathrm{AMA}V_{p_i}$ and c) $\mathrm{AMA}\gamma_{p_i}$ indices evaluated at the 39 locations depicted in Figure 2.1.

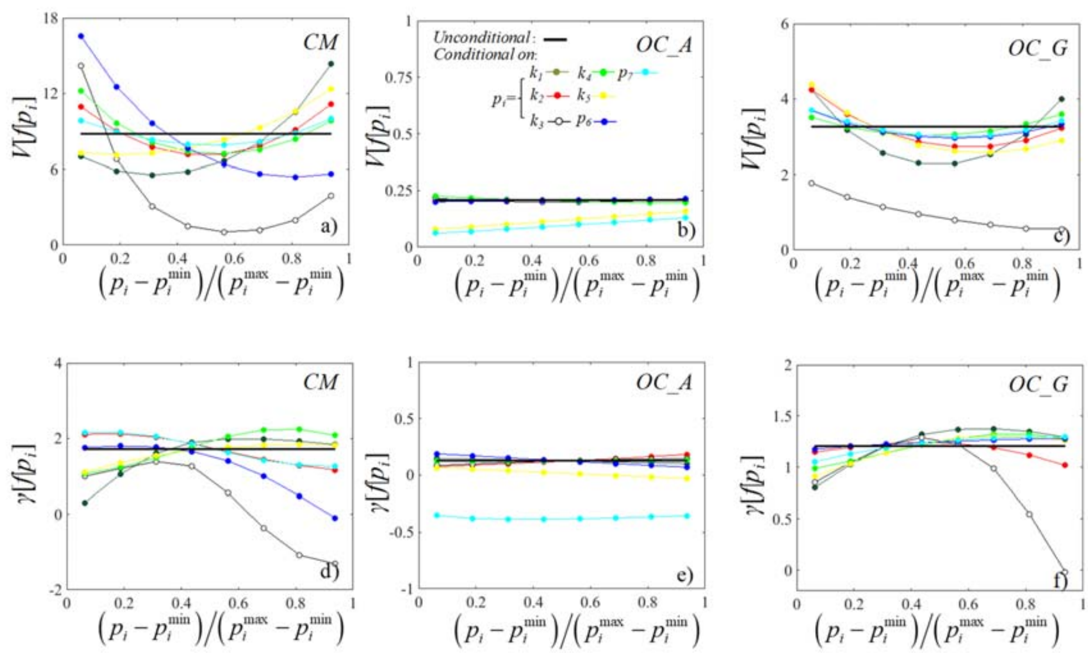

Figure 2.5. Conditional a-c) variance $V\left[f|p_i\right]$ and d-e) skewness $\gamma\left[f|p_i\right]$ versus normalized p_i at a selected observation well (ID 32; see Figure 2.1) for the conceptual models considered. The corresponding unconditional moments (horizontal black lines) are also shown. Results are obtained

via 2 × 10^6 runs of the gPCE-based surrogate model subdividing each parameter interval into eight uniform bins.

In order to provide an overall assessment of model parameter impacts on hydraulic heads across the domain, we compute the average of each sensitivity index across all 39 locations considered (the averaging operator is hereafter denoted with symbol $\langle\ \rangle$). In this analysis we consider also Morris, $\overline{\mu}^*_{p_i}$, and Sobol, $S^T_{p_i}$, metrics evaluated in Deliverable 1.4a. Figure 2.6a depicts $\langle S^T_{p_i} \rangle$ versus $\langle \overline{\mu}^*_{p_i} \rangle$ for the model conceptualizations analysed. These two traditional sensitivity measures display the following consistent trends (only a few minor differences in term of ranking of parameter importance can be detected): (*i*) hydraulic head for all conceptual models are significantly affected by the uncertainty of k_3 and k_5, while the effects of k_2 and k_4 are always negligible; (*ii*) the strength of the influence of the uncertainty of k_1 depends on the conceptual geological model adopted and is negligible in *OC_A*; (*iii*) *CM* and *OC_A* are more affected by the uncertainty in the Dirichlet (as quantified by p_7) than in the Neumann (i.e., p_6) boundary condition, the opposite behavior being observed for *OC_G*.

The scatterplot of $\langle \mathrm{AMA}V_{p_i} \rangle$ versus $\langle \mathrm{AMA}E_{p_i} \rangle$ values is depicted in Figure 2.6b. We note that mean values of hydraulic heads in *OC_G* are more affected by uncertainty in a few selected parameters (k_1, k_3, k_5, and p_6) with respect to what can be observed for *OC_A* and *CM* (note the isolated cluster of green symbols, diamonds, in Figure 2.6b). Conversely, hydraulic head variance is affected by uncertainty of input parameters in a similar way for the three considered models (i.e., all three models lead to comparable values of $\langle \mathrm{AMA}V_{p_i} \rangle$). Comparing $\langle \mathrm{AMA}V_{p_i} \rangle$ and $\langle S^T_{p_i} \rangle$ (Figure 2.6c), enables us to further support our previous observation that the impact of some parameters (e.g., p_6, k_4 and k_2 for *CM* and k_4 and k_2 for *OC_G*) on output hydraulic head variance cannot be fully appreciated by the $\langle S^T_{p_i} \rangle$ indices. Figure 2.6d depicts $\langle \mathrm{AMA}V_{p_i} \rangle$ versus $\langle \mathrm{AMA}\gamma_{p_i} \rangle$. We note that all points tend to follow a linear trend of unit slope for *CM* and *OC_A*, suggesting that uncertainty on model parameters affect variance and skewness of output hydraulic heads in a similar way. Otherwise, considering *OC_G* we note that the influence of some parameters (k_1, k_5 and p_6) decreases for increasing order of the (statistical) moment of the output head distribution.

2.1.3 Conclusions

In Deliverable D1.4a and in the present document we compare a set of Global Sensitivity Analysis (GSA) approaches to evaluate the impact of conceptual geological model and parametric uncertainty on groundwater flow features in a three-dimensional large scale groundwater system. Our work leads to the following major conclusions.

1. Albeit being based on differing metrics and concepts, the three GSA approaches analyzed lead to similar and (generally) consistent rankings of parameters which are influential to the target model outcomes at the set of investigated locations. Otherwise, the choice of the conceptual model employed to characterize the lithological reconstruction of the system affects the degree of influence that uncertain parameters can have on modeling results.
2. When considering the overall behavior of model responses across the set of observation points, all GSA indices suggest that geomaterials constituting a relatively modest fraction of the aquifer (~10÷15%) are influential to hydraulic heads only if they are associated with large conductivities. Otherwise (i.e., if their conductivity has a low to intermediate value), these geomaterials are not influential in any of the geological models considered.
3. The impact of very low conductivity geomaterials (such as those associated with facies No. 1 in Table 2.1 of Deliverable 1.4a) depends on the conceptual model adopted when their volumetric fraction is significant (~30%). These geomaterials do not influence the variability of hydraulic heads computed through the *OC_A* model (Overlapping Continuum scheme associated with arithmetic averaging of geomaterial conductivities). Otherwise, they are seen to be remarkably influential for the *CM* (Composite Medium) model and the *OC_G* (Overlapping Continuum scheme associated with geometric averaging of geomaterial conductivities) model.
4. Uncertainty in the Neumann boundary condition plays only a minor role with respect to the Dirichlet boundary condition, which strongly controls variability of hydraulic head, in the *CM* and *OC_A* models. The opposite behavior is observed for the *OC_G* approach.
5. The moment-based indices AMAE, AMAV, and AMAγ (which quantify the impact of model parameters on the mean, variance, and skewness of the pdf of model outputs, respectively) suggest that all model parameters affect in a similar way mean, variance and skewness of hydraulic heads for the *CM* and *OC_A* approaches. When considering the *OC_G* conceptualization, we note that some of the influential parameters (i.e., the largest/smallest geomaterial conductivities, and Neuman boundary conditions) influence the mean of hydraulic heads more strongly than its variance or skewness.
6. The degree of symmetry of the pdf of hydraulic heads, as quantified by the skewness, depends on the considered conceptual model and varies across the domain. Conditioning on model parameters markedly affects the shape of the pdf of heads, whose degree of symmetry can strongly depend on conditioning parameter values.
7. Evaluation of the AMAV indices for the *CM* and *OC_G* conceptualizations suggests that the importance of the influence of some parameters on head variance is underrepresented by the Sobol' indices. This is related to our finding that the variance

of the model output conditional on these parameters is not always smaller that its unconditional counterpart. This (*a*) hampers the ability of the Sobol' indices to completely detect the effect of these parameters on the model output variance, and (*b*) leads to different ranking of model parameters considering either the AMA*V* or the Sobol' metrics.

Our results form the basis for the development of an efficient parameter estimation that is described in Section 2.2. Parameters which have been identified as noninfluential to model outcomes (as expressed through their key statistical moments) can be neglected in the model calibration process and fixed to given values.

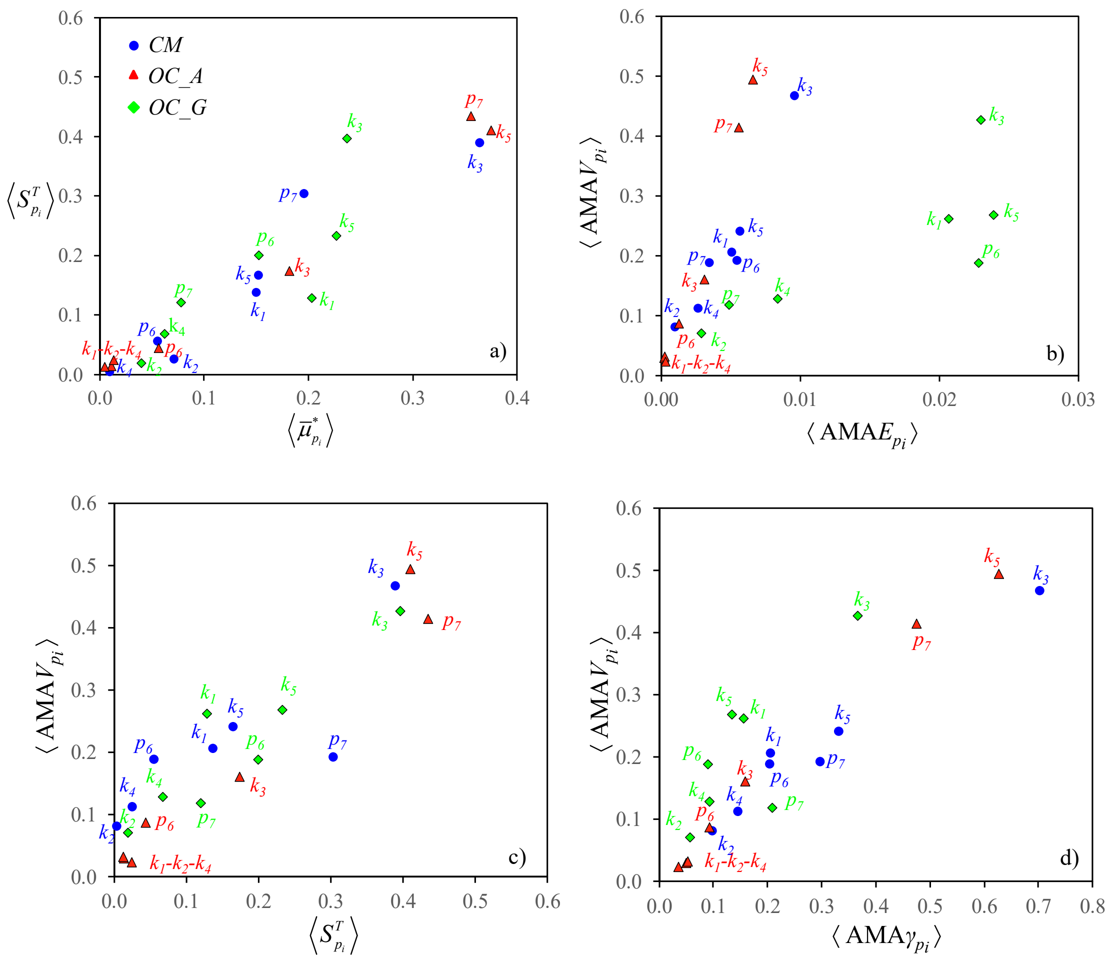

Figure 2.6. Scatterplots of sensitivity indices averaged across all 39 target locations. a) averaged total Sobol indices $\langle S_i^T \rangle$ versus averaged scaled Morris Index $\langle \bar{\mu}_i^* \rangle$; b) $\langle \mathrm{AMA}V_{p_i} \rangle$ versus $\langle \mathrm{AMAE}_{p_i} \rangle$; c) $\langle \mathrm{AMA}V_{p_i} \rangle$ versus $\langle S_i^T \rangle$; d) $\langle \mathrm{AMA}V_{p_i} \rangle$ versus $\langle \mathrm{AMA}\gamma_{p_i} \rangle$. Blue circles, red triangles, and

green diamonds correspond to results obtained via the *CM*, *OC_A* and *OC_G* conceptual models, respectively.

2.2 Natural spring modelling and model calibration

According to the results of the GSA, in Deliverable 1.4a, we calibrate parameters k_1, k_3 and k_5 for *CM* and *OC_G* models and k_3, k_5 for *OC_A*. For each conceptual model, insensitive parameters are fixed to values consistent with the geological features of the corresponding classes, as reported in Table 2.5 of Deliverable 1.4a. As calibration data, we considered yearly-averaged hydraulic heads collected at each observation well during year 2015 (location of these wells is reported in Figure 2.1 and Annex I).

Here, we focus on the calibration of an additional model parameter which is the spring leakage coefficient. The latter, as we detail below, is the main parameter affecting the spring outflow rate predicted by the numerical models.

2.2.1 Methodology

A key feature of the Cremona aquifer system is the presence of high quality water springs. In the numerical model these springs are simulated as drains. We consider a set of 138 springs (the list is reported in Annex II). The specific outflow-rate per unit area of the i-th drain, $q_{d,i}$ [LT^{-1}], is modelled as

$$q_{d,i} = \begin{cases} -\dfrac{K_d}{e}\left(h_i - h_{0,i}\right) & h_i > h_{0,i} \\ 0 & h_i \le h_{0,i} \end{cases} \tag{2.3}$$

where h_i [L] and $h_{0,i}$ [L] are, respectively, the hydraulic head and the elevation of ground level, at the i-th drain, K_d [LT^{-1}] and e [L] being are the hydraulic conductivity and the thickness of the drain bed. Since no information are available about the spatial variability of K_d and e, they are assumed constant (in space). Quantities K_d and e allow to evaluate leakage coefficient l_d [T^{-1}]

$$l_d = K_d / e \tag{2.4}$$

The total discharge, Q_d [L^3T^{-1}] outflowing from the whole set of drains in the model can be evaluated as:

$$Q_d = A\sum_{i=1}^{N_D} q_{d,i}$$

where A [L^2] is the planar area of the drain and N_D is the number of drains considered. The estimation of the leakage coefficient is cumbersome (Doppler et al., 2007). It can be locally measured (Kaleris, 1998) but it is usually calibrated making use of hydraulic head data and/or flow rate measurements (when available).

For the Cremona aquifer the following measurements of spring flow rates are available:

a) A campaign of Consorzio della Media Pianura Bergamasca, CMPB, (Maione et al., 1991) recorded discharge measurements at 35 sections of channels collecting water flowing out from the springs within the study area (see Fig. 2.7). Measurements have been performed during the years 1989-1990 on a (approximately) bi-monthly basis. The list of the total discharge measurements over the 35 sections is reported in Annex III.
b) Flow rate measurements performed at four locations along the three main channels (named Misana, Quarantina and Acquarossa). Measurements have been collected on a (approximately) weekly basis, during the irrigation period, from 31/03/2009 to 2/09/2009 from Consorzio Irrigazioni Cremonesi and Consorzio Adda-Serio. The complete set of available measurements is reported in Annex III.

The first set of spring flow rate measurements (a) is representative of a significantly larger area of the investigated domain with respect to the second set (b). For this reason, set (a) has been used to calibrate l_d by means of a Maximum Likelihood method (described in Section 2.4.1 of Deliverable 1.4a). We assume that only springs located upstream of the measurement sections contribute to the measured flow rate.
The second set of measurement (b) has been adopted, at the end of the inversion procedure, for validation purposes.

The calibration has been performed according to the following iterative procedure:

i) hydraulic conductivity values are calibrated using hydraulic head measurements considering a first attempt value of the leakage coefficient (this step has been performed in Deliverable 1.4a);

ii) leakage coefficient is calibrated using the spring flow rate measurements collected by CMPB (1989-1990), fixing hydraulic conductivities at the optimal values obtained at the previous step;

iii) hydraulic conductivity values are re-calibrated using the optimal leakage coefficient obtained at point (*ii*).

The method converges in few steps leading to optimal values of hydraulic conductivity and leakage coefficient obtained on the basis of both hydraulic head and spring flow rate measurements.

In Deliverable 1.4a, during the calibration of hydraulic conductivity values, Dirichlet and Neumann boundary conditions investigated during the sensitivity analysis were fixed to three selected constant values representing the lower bound, medium behavior and upper bound of their range of variability (see Table 2.3 of Deliverable 1.4a). The considered sets of boundary conditions have been called BC_1, BC_2 and BC_3.

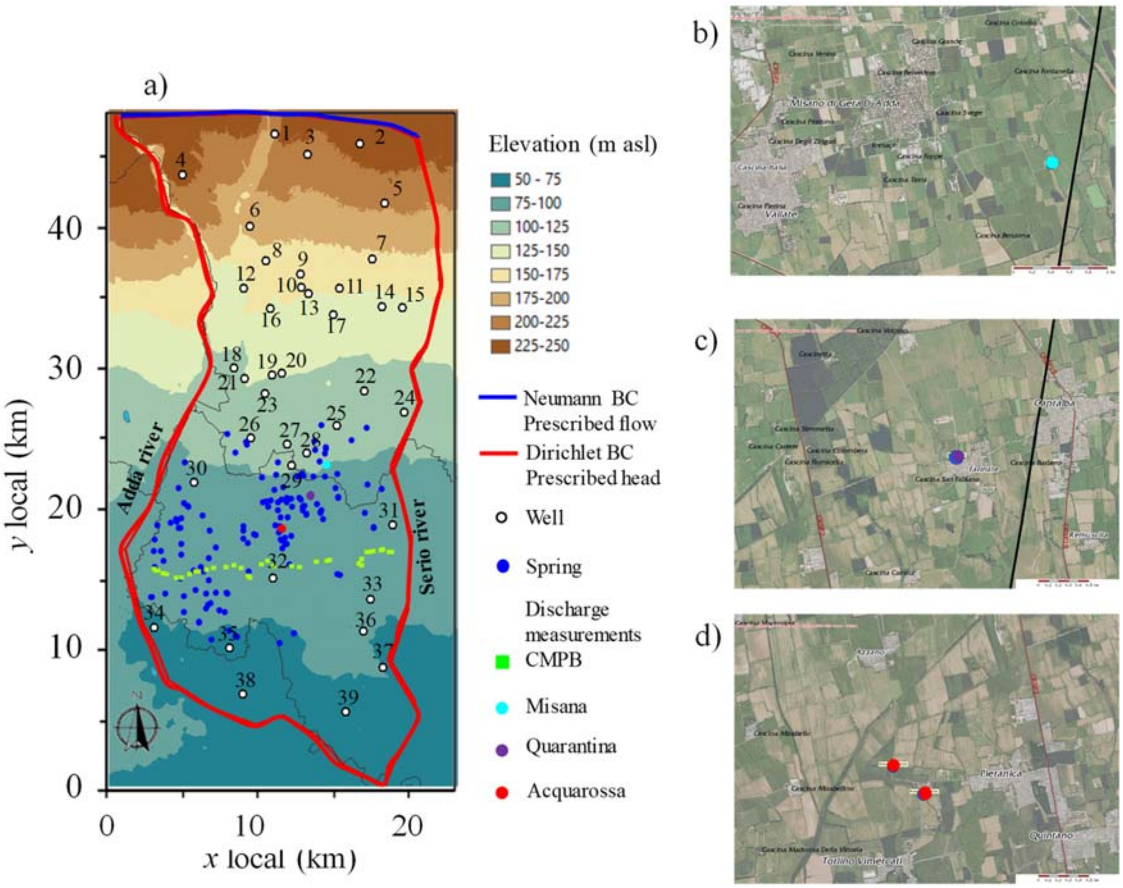

Figure 2.7. a) Location of natural spring and spring flow rate measurements within the study area. A zoom-in of the measurement locations is also reported for: b) Misana, c) Quanrantina and d) Acquarossa (upstream and downstream) channel.

2.2.2 Results and discussion

Table 2.1 reports the value of the leakage coefficient at the end of the inversion process for the three conceptual models, i.e. *CM*, *OC_A* and *OC_G*. These results are associated with boundary conditions set BC_3 (i.e. p_6 = 19.30 m^3/s and p_7 = 3.0 m) corresponding to the best optimization results for *CM* and *OC_A* (see Table 2.4 of Deliverable 1.4a). Considering *OC_G,* results associated with BC_3 allow to obtain the best match between total spring flow rate measured and predicted by the model. For the three investigated model conceptualizations the spring leakage coefficient assumes value consistent with the study of Doppler et al. (2007) which calibrate leakage coefficients in the context of rivers-aquifer interaction. The estimated leakage coefficients are similar in the three models, the highest value being associated with the *CM* approach. All the three model approaches can render values of Q_d closed to the mean measured counterpart (= 14.62 m^3/s).

Parameter	Symbol	*CM*	*OC_A*	*OC_G*	Unit
Leakage coefficient	l_d	0.15	0.12	0.11	day^{-1}
Leakage coefficient	l_d	$1.72{\times}10^{-6}$	$1.33{\times}10^{-6}$	$1.25{\times}10^{-6}$	s^{-1}
Total spring flow rate	Q_d	14.73	14.61	14.64	$m^3\,s^{-1}$

Table 2.1. Values of leakage coefficient and simulated total spring discharge.

Values of *J* (squared difference between measured and predicted hydraulic head), σ_h^2 (ML estimates of the variance of measurement errors of *h*) and model discrimination criteria NLL, AIC, AICc, BIC, KIC (see Deliverable D1.4a for details) evaluated at the end of the inversion procedure for the three conceptual models are reported in Table 2.2. Minima amongst all models are in bold. Values of *J* converge to a smaller value in *CM*. Model identification criteria tend to favour *OC_A,* based on the principle of parsimony, because it has less parameters with respect all remaining models. Our results confirm what we found in Deliverable 1.4a where we note that *OC_A* seems to provide a more robust model with respect to the *OC_G* approach and the *CM* model.

	CM	*OC_A*	*OC_G*
J	**1529**	1558	1587
σ_h^2	39.21	39.95	40.69
NLL	**253.8**	254.5	255.2
AIC	259.8	**258.5**	261.2
AICc	260.4	**258.8**	261.9
BIC	264.8	**261.8**	266.2
KIC	256.9	**256.4**	260.5

Table 2.2. Inversion statistic for the three conceptual models and model identification criteria. Minima amongst all models are in bold.

Conductivity estimates of each facieas are reported in Table 2.3 for the three conceptual models. The estimation error standard deviation, SD, calculated according to the ML methodology, is also reported for all estimated parameters. The hydraulic conductivity estimated values are consistent with the geological features of the classes and are very close to those obtained in Deliverable 1.4a before the calibration of leakage coefficient. For all conceptual models, the lowest value is associated with the clay, silt and fine sand materials, corresponding to Classes 1 and 2, while the largest conductivities are related to gravel material and the fractured conglomerate, corresponding to Classes 3 and 5. Figure 2.8 depicts simulated versus observed hydraulics heads for the three calibrated models.

	CM		*OC_A*		*OC_G*	
	k	SD	*k* (m/s)	SD	*k* (m/s)	SD
k_1 (m/s)	5.81×10^{-5}	2.95×10^{-5}	1.00×10^{-6}	-	9.34×10^{-5}	1.68×10^{-5}
k_2 (m/s)	1.00×10^{-4}	-	1.00×10^{-4}	-	1.00×10^{-4}	-
k_3 (m/s)	1.10×10^{-2}	4.31×10^{-3}	1.84×10^{-2}	4.91×10^{-3}	5.44×10^{-2}	2.49×10^{-2}
k_4 (m/s)	1.00×10^{-5}	-	1.00×10^{-5}	-	1.00×10^{-5}	-
k_5 (m/s)	4.71×10^{-3}	1.79×10^{-3}	4.44×10^{-3}	1.88×10^{-3}	3.27×10^{-2}	1.53×10^{-2}

Table 2.3: Parameter estimates and related estimation error standard deviation for the three conceptual models analysed.

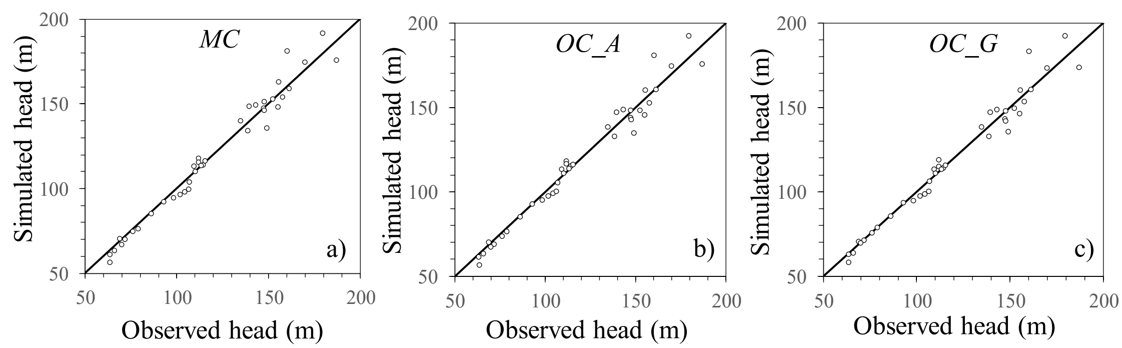

Figure 2.8. Simulated versus observed hydraulic head at monitoring stations. Simulated heads have been obtained with the a) *CM*, b) *OC_A* and c) *OC_G* approaches.

2.2.3 Model validation

Model validation is performed upon comparing the local measured values of spring flow rate (Acquarossa upstream and downstream, Quarantina and Misana) not used in the inversion procedure against the outflow rate predicted on the basis of the best set of parameters identified in the previous Section for the three conceptual models (see Figure 2.7 b-d for the location of the validation points). Figure 2.9 depicts measured and predicted flowrates at the four locations adopted during the validation procedure. The flow rates measured at Acquarossa upstream and downstream are closely reproduced by their model estimates, while some discrepancies can be observed among measured and estimated values of Q_d at Misana and Quarantina sections.

This finding can be related to the following reasons: (*i*) our models provide an estimate of the mean annual flow rate at the springs while measurements have been collected only during the irrigation period; (*ii*) heterogeneity on the drain characteristics are neglected.

However, we note that the developed model is accurate in reproducing the behavior of the main flow feature of the site (e.g., hydraulic heads and mean annual total discharge at the drains).

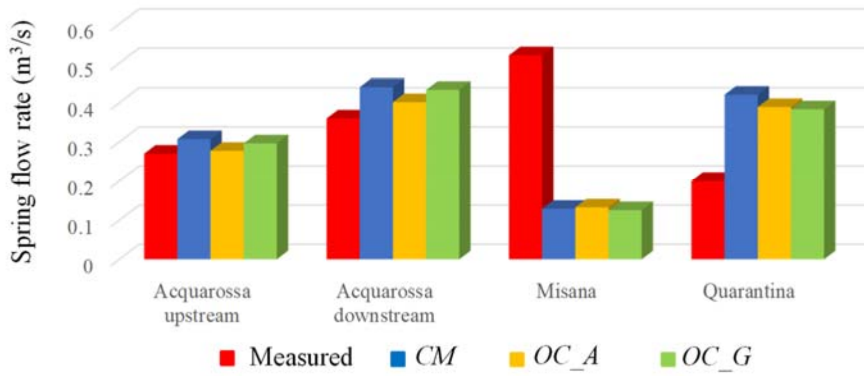

Figure 2.9. Measured and predicted spring flow rate at four locations (Acquarossa upstream, Acquarossa downstream, Misana and Quarantina).

3. Bologna site

The Bologna aquifer system is located in the medium alluvial Po Plain. The investigated domain extends over 20 × 23 km^2 in the horizontal plane and from -450 m to 100 m a.s.l. along the vertical direction. The system is discretized into N_{tot} = 40 × 46 × 110 cells of uniform size of 500 m × 500 m × 5 m. Lithological data available from more than 1300 boreholes allowed to identify 4 main categories within the area: clay, gravel, silt and sand, with volumetric fraction $p_1 = 0.523$, $p_2 = 0.281$, $p_3 = 0.133$ and $p_4 = 0.063$ respectively. As detailed in Deliverable 1.4a, we apply two diverse geostatistical reconstruction techniques to describe the architecture of the aquifer system: SISIM, a classic sequential-indicator approach (Deutsch and Journel, 1992) and TPROGS, a transition-probability based method (Carle and Fogg, 1996, 1997). The two techniques are compared in a Monte Carlo (MC) framework, by relying on two sets of n = 100 realizations conditioned on lithological data. In Deliverable 1.4a, we computed ensemble indicator variograms and transiograms evaluated over each set of MC realizations. We observed that: (*i*) all ensemble variograms, γ_{I_k}, and transiograms, t_{jk}, converge to their theoretical values, respectively $p_k(1-p_k)$ and p_k; (*ii*) for all facies, TPROGS-based ensemble variograms are characterized by larger horizontal and vertical ranges compared to their SISIM counterparts; (*iii*) TPROG-based ensemble transiograms reach the plateau for larger separation distance with respect to SISIM counterparts. Figures 3.1 and 3.2 depict facies distributions over a vertical cross section in one realization generated with SISIM and TPROGS respectively. A qualitative comparison of these figures reveals that the SISIM simulations are characterized by a more fragmented facies distribution than TPROGS counterparts. To investigate this aspect quantitatively, in the following sub section we characterize the connectivity of facies in our systems.

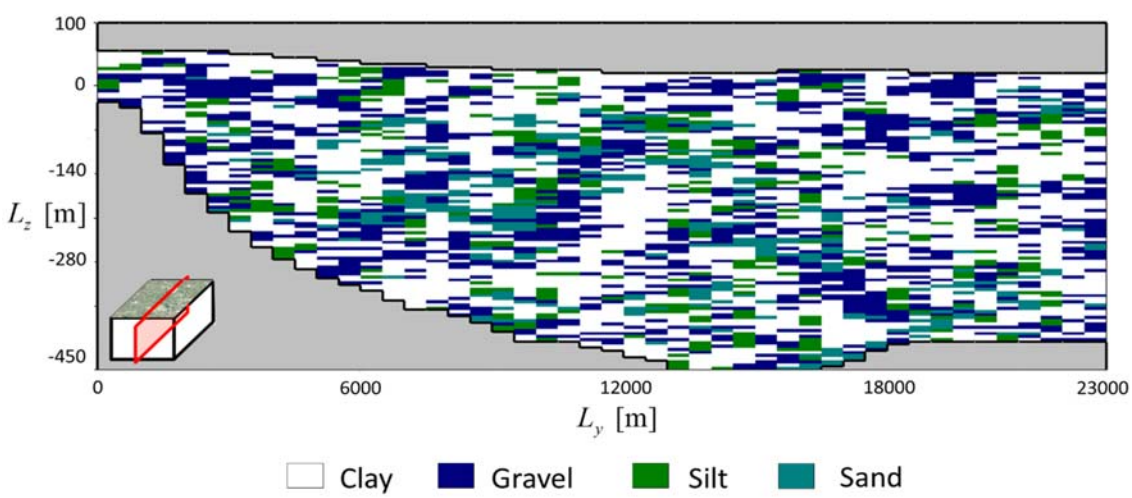

Figure 3.1. Facies distribution along a vertical cross section in one realization generated with SISIM.

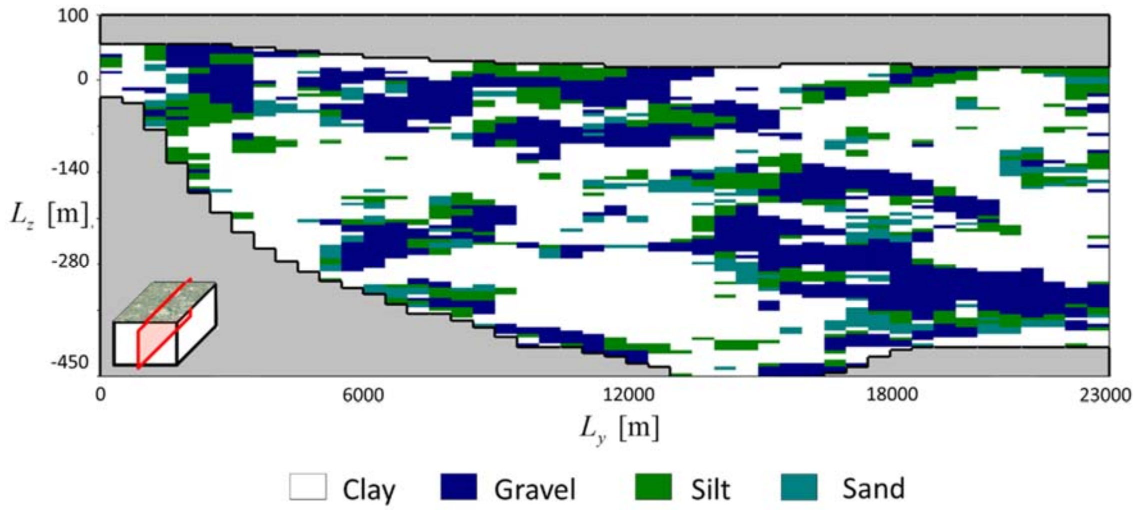

Figure 3.2. Facies distribution along a vertical cross section in one realization generated with TPROGS.

3.1 Investigation of connectivity metrics

Predictions of flow and transport processes in aquifer systems are critically affected by their intrinsically heterogeneous nature (Neuman, 2008; Neuman and Di Federico, 2003), including the spatial arrangement of the hydraulic properties, a prominent role being played by a feature typically denoted as connectivity (Knudby and Carrera, 2005, Renard and Allard, 2013). A formal and unambiguous definition of connectivity is still lacking. Connectivity can be regarded as a measure of the presence of preferential flow paths that enable fast flow and transport throughout the system. Understanding the mechanisms driving flow to concentrate in high-velocity channels is key for proper prediction of first arrival times of dissolved chemicals at critical targets (Cvetkovic et al., 2014; Henry et al., 2015; Zinn and Harvey, 2003), with direct implications in environmental risk assessment. In this context, our goal is to evaluate quantitatively (*i*) the connectivity of the diverse facies in each realization, (*ii*) the variability of connectivity within a set of equally-likely facies distributions, and (*iii*) the extent at which the generation method affects facies connectivity.

In order to define any connectivity metric, some basic definitions must be introduced. Our three-dimensional domain is discretized by a regular cubic grid, in which each cell has 6 neighbors. Let Ω_k be the subset of grid cells that are associated with the *k*-th geomaterial. Two cells, $\mathbf{x}_A$ and $\mathbf{x}_B$, of Ω_k are said to be connected if there exist a sequence of neighboring cells from $\mathbf{x}_A$ to $\mathbf{x}_B$ that is completely included in Ω_k. A group of connected cells is called a "cluster". A first set of connectivity metrics can be inferred from the analysis of clusters. As illustrated by Lee et al. (2007), useful indicators are: (*i*) N_C, the total number of clusters identified within the system; (*ii*) $C_{\max}$, the number of cells in the largest cluster divided by the total number of cells of the domain, N_{tot}; (*iii*) N_I, the number of isolated cells, i.e., cells belonging to Ω_k not connected to any other cell of Ω_k. These indices have been computed for each geomaterial (or category) and in each realization for both generation methods. The results are reported in Figure 3.3 in the form of boxplots, to visualize both average values and ranges of variation of the indices. Figure 3.3a collects the boxplots of N_C, highlighting that all facies are considerably more fragmented in SISIM than in TPROGS. This holds in particular for gravel, whose average number of clusters differ by almost one order of magnitude between the two generation methods. Figure 3.3a also shows that, in SISIM, N_C is characterized by a wide variability and also by the presence of outliers in the distributions (depicted as red circles). The results obtained for $C_{\max}$ are reported in Fig. 3.3b. The two facies with the largest volumetric fraction (clay and gravel) are characterized by considerably larger clusters with respect to the other two (silt and sand). It can be also noted that, with both methods, the mean value of $C_{\max}$ for clay is very close to its total volume fraction, p_1, indicating that this category is essentially made by one single cluster. The same holds for gravel in TPROGS-based realizations and, to a lesser extent, for the SISIM set. This denotes that, with the latter generation method, there is a non-negligible portion of gravel cells that are not connected to the predominant cluster. Moreover, as it can be observed comparing the boxplots of N_I (Fig. 3.3c), gravel has the largest number of isolated cells when we consider the SISIM set. This clarifies that gravel cells outside the main cluster are not connected with each other in SISIM simulations.

As emphasized by Renard and Allard (2013) and references therein, connectivity metrics can be effectively interpreted in the framework of percolation theory. This theory was originally formulated for uncorrelated Bernoulli random fields defined on infinite domains (i.e., on grids extending over a distance much larger than the grid step): in any node of the grid, the field can be either 1 or 0 with probability *p* and (1-*p*) respectively. A single realization would hence be made by Ω_1, i.e., the set of grid cell where the field is equal to 1, and its complementary set, Ω_0. The basic principle of percolation theory is that there exists a critical value of *p*, called *percolation threshold* (p_t), such that the probability for Ω_1 to form a unique cluster is equal to 1 if $p \geq p_t$ and equal to 0 if $p < p_t$. The theory also allows to prove that the value of p_t decreases with the increase of (*i*) the grid dimension and (*ii*) the number of neighbors of a grid cell. For a three-dimensional cubic grid with 6 neighbours, $p_t = 0.31$ (Stauffer and Aharony, 1992).

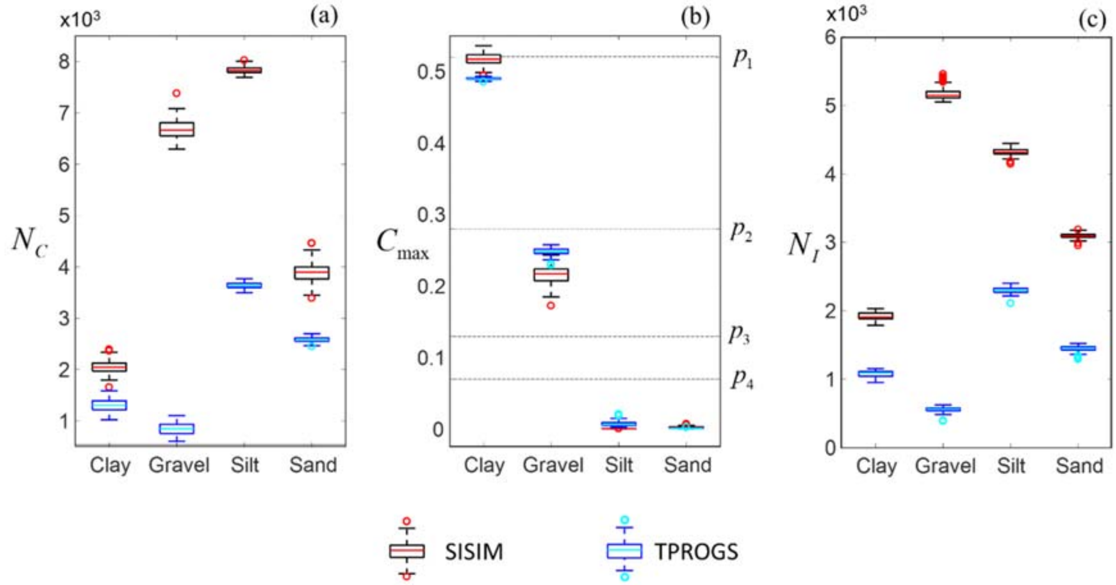

Figure 3.3. Boxplot of the connectivity indices (a) N_C (b) $C_{\max}$ and (c) N_I computed for each category over all 100 realizations generated with SISIM (black and red symbols) and TPROGS (blue and cyan symbols). In (b), the proportion of each category in the domain is also indicated by horizontal dashed lines.

Application of the percolation theory to our problem implies that there exists a threshold value of the volumetric proportion of a facies above which this facies is *most likely* made by a unique cluster spanning over the whole grid. Here we use the term "most likely" to indicate that the investigated domain differs from the one considered in the theoretical framework for being (*i*) finite and (*ii*) spatially correlated. As a consequence, the probability of occurrence of a percolating cluster is not a step function but increases gradually from 0 to 1 over a range of values of *p* centered on the theoretical p_t of the system. As illustrated by Hovadik and Larue (2007), this range gets wider as the domain departs from the theoretical conditions, i.e., as the number of grid cells decreases and as the facies correlation length increases. Moreover, as it can be intuitively seen, spatial correlation enhances connectivity, resulting in a decrease of p_t below the theoretical value of 0.31. The results observed for the connectivity indices are consistent with this theoretical framework, since: (*i*) TPROGS set, which exhibits larger correlation lengths than SISIM counterparts for all categories, shows a higher degree of connectivity than SISIM, as measured by the smaller N_C and N_I values displayed; (*ii*) SISIM realizations are characterized by a larger variability in the category proportions $\left(O\left(10^{-3}\right)\right)$ with respect to TPROGS $\left(O\left(10^{-5}\right)\right)$, which implies a higher variability in connectivity metrics; (*iii*) being the volumetric fraction of clay $p_1 > p_t$, this category has a probability ≈ 1 to form a unique percolating cluster; (*iv*) silt and sand proportions, p_3 and p_4, are far below the percolation threshold and their correlation lengths are very short (< 5 cells, see Deliverable 1.4a). So, for these categories it is extremely unlikely to form long clusters; (*v*) gravel is correlated over a long distance (>10 cells). This makes its volumetric proportion, p_2, large enough for a percolating cluster to occur. However, the fact that p_2 is close to the percolation threshold results in a high variability of the connectivity of this category from one realizations to the other. This issue can be highlighted by evaluating the connectivity function (Renard and Allard, 2013, Vassena et al., 2010), i.e. the probability for two cells in the same category, separated by a given distance, to be connected. The connectivity function, $\tau_k^j\left(h\right)$, between cells belonging to category *k* and separated by distance *h* along direction *j*, with *j* ={*x*, *y*, *z*} can be computed as:

$$\tau_k^j\left(h\right)=\frac{N\left(\mathbf{x}_A\leftrightarrow\mathbf{x}_B\middle|\mathbf{x}_A\in\Omega_k,\mathbf{x}_B\in\Omega_k,\mathbf{x}_A-\mathbf{x}_B=h\mathbf{e}_j\right)}{N\left(\mathbf{x}_A\in\Omega_k,\mathbf{x}_B\in\Omega_k,\mathbf{x}_A-\mathbf{x}_B=h\mathbf{e}_j\right)} \tag{3.1}$$

where $N\left(\mathbf{x}_A\in\Omega_k,\mathbf{x}_B\in\Omega_k,\mathbf{x}_A-\mathbf{x}_B=h\mathbf{e}_j\right)$ indicates the number of pairs of cells, $\left(\mathbf{x}_A,\mathbf{x}_B\right)$, belonging to category *k* that are separated by the distance *h* along direction *j* and $N\left(\mathbf{x}_A\leftrightarrow\mathbf{x}_B\middle|\mathbf{x}_A\in\Omega_k,\mathbf{x}_B\in\Omega_k,\mathbf{x}_A-\mathbf{x}_B=h\mathbf{e}_j\right)$ is the number of those pairs which also belong to the same cluster (this condition being expressed by $\mathbf{x}_A\leftrightarrow\mathbf{x}_B$). Note that $\tau_k^j\left(0\right)=1$. The behavior of τ_k^j as the separation distance increases can be predicted by percolation theory: for $p_k<p_t$, the curve τ_k^j versus *h* decreases rapidly to 0, following an exponential trend (Grimmett, 2000); for $p_k>p_t$, τ_k^j tends asymptotically to a constant (non-zero) value, which is the square of the probability for a cell in category *k* to belong to the percolating cluster. In our case, $\tau_{k,\infty}=\left\langle\left(C_{\max}^k/p_k\right)^2\right\rangle$, where the brackets represent the average over all realizations.

Figure 3.4 collects connectivity function curves evaluated along *x*, *y* and *z* axes for each single realization in both the generated sets (dotted lines). The figure also displays the ensemble connectivity functions (solid lines) evaluated over the whole 100 realizations. We can recognize the behavior expected for $p_k<p_t$ in the curves of silt and sand. In particular, Fig. 3.4 reveals that, while in SISIM fields the connectivity of sand is larger than the connectivity of silt, the opposite occurs in fields generated by TPROGS. This result emphasizes the role of spatial correlation on connectivity: SISIM generations are based on the variogram model inferred from conditioning data. The horizontal range of the sand variogram model is larger than its counterpart for silt (see Deliverable D1.4a).

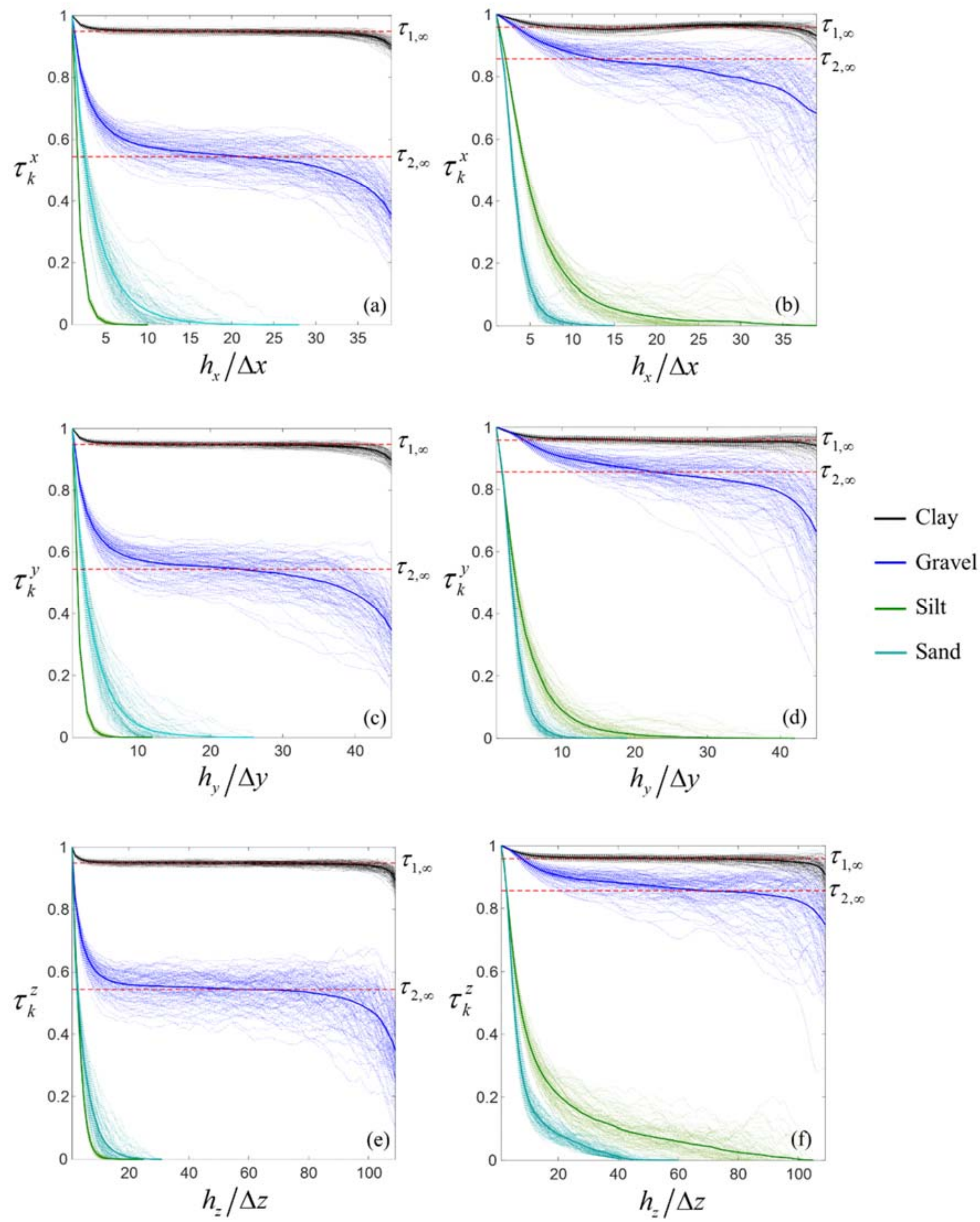

Figure 3.4. Ensemble connectivity function versus separation distance along *x* (a-b), *y* (c-d) and *z* (e-f) axes evaluated, for each category, over all 100 realizations (solid lines) generated with SISIM (a-c-e) and TPROGS (b-d-f). Connectivity functions computed in each single realization are also reported (dotted lines).

We also note that, for large separation distances, the curves τ_k^j for clay and gravel tend to non-zero values. The latter tend to coincide with the expected asymptotic value $\tau_{1,\infty}$ for clay, while it is smaller than $\tau_{2,\infty}$ for gravel. This discrepancy is probably due to the effect of a non-infinite extension of the domain. The most relevant difference between the two generation methods concerns gravel, which attains considerably larger values of τ_k^j for TPROGS (Fig. 3.4b-d-f) with respect to SISIM (Fig. 3.4a-c-e). This can be motivated by the fact that, as we observed from the connectivity indices, in SISIM realizations gravel is more fragmented. So, the probability for a cell to belong to the percolating cluster is smaller, and, in turn, the asymptotic value associated with the curve decreases. Figure 3.4 also highlights that, as discussed above, gravel is characterized by a remarkably wider variability compared to the other categories for both methods. Since gravel is also the most conductive facies in our domain, this variability may have a serious impact on groundwater flow. This aspect will be further discussed in the next sections.

3.2 Groundwater numerical model

We consider all 100 realizations of facies distribution generated with SISIM and with TPROGS. For each realization, we develop a steady state, three-dimensional groundwater flow model. In Deliverable 1.4a, we introduced the numerical code used to simulate groundwater flow. To improve the accuracy of calibration results, the numerical model described in Deliverable 1.4a has been modified as follows:

(*i*) We modified the surface recharge, *R*, including information on land use as:

$$R = P - Q - E + L \tag{3.2}$$

where *P* is the rainfall, *Q* is the surface runoff (soil-use dependent, calculated on the basis of the curve number method), *E* is the evapotranspiration term and *L* quantifies water-pipe losses in the urban areas (15% of the usage, calculated on the basis of population density data). The spatial distribution of recharge obtained from (3.2) is depicted in Fig. 3.5a.

(*ii*) In the former version of the model, we merged all pumping wells located within each municipality in a single cell. As it is shown in Fig. 3.5b, some pumping wells (black symbols) are very close to head-observation wells used for model calibration (red symbols). Therefore, in the new model, we locate each pumping well in the exact position.

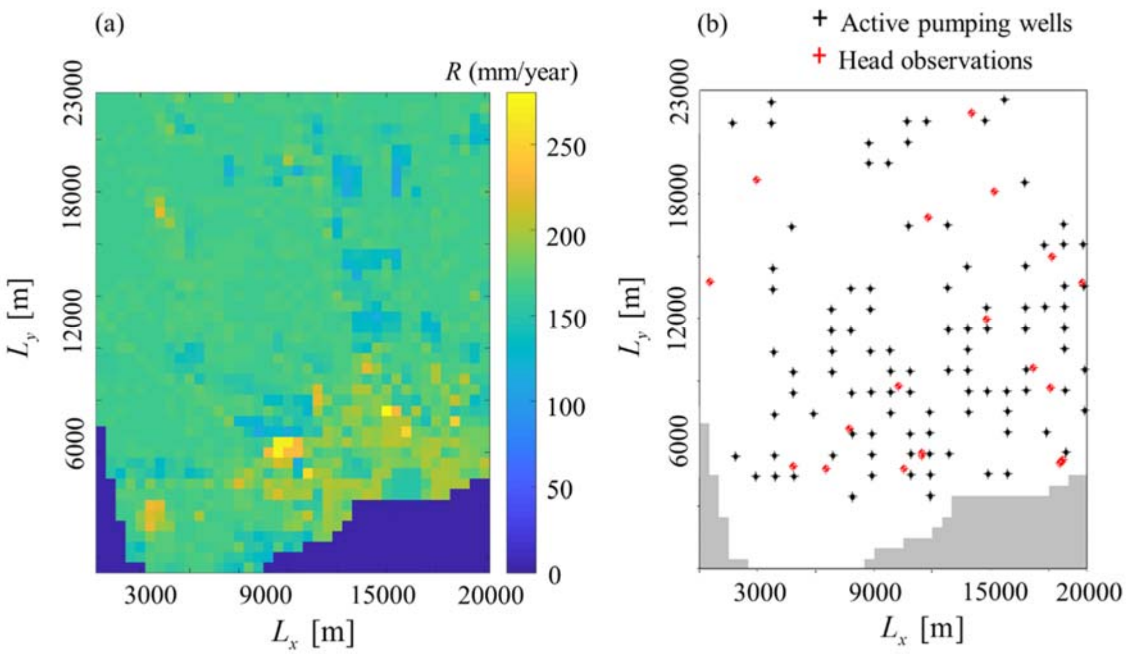

Figure 3.5. (a) Contour map of surface recharge. (b) Location of pumping (black symbols) and monitoring (red symbols) wells within the domain of simulation.

3.3 Model Calibration

Hydraulic conductivity values associated with the diverse geomaterials are calibrated in each MC realization on the basis of a Maximum Likelihood approach. As calibration data, we consider yearly-averaged hydraulic heads collected at 20 wells, the location of which is included in Figure 3.5b. As discussed in Deliverable 1.4a, hydraulic conductivity values associated with the two categories with the smallest volume fraction – i.e., silt and sand – do not affect appreciably the model outcomes. Therefore, reliable estimates of k_3 and k_4 cannot be obtained with the available data and we fix k_3 = 10^{-6} m/s and k_4 = 10^{-5} m/s, corresponding to intermediate characteristic values for the geomaterial considered.

Figures 3.6a and 3.6b collect the calibrated values of clay hydraulic conductivity, k_1, obtained in each realization of (a) SISIM and (b) TPROGS. The 95% confidence intervals (CIs) associated to each estimate are also reported in the figures. It can be noted that the results of the SISIM set are generally larger and characterized by larger estimation errors (as quantified by the 95% CI) than those of the TPROGS set. The same happens for gravel conductivity values, k_2, depicted in Figs. 3.6c and 3.6d. These results are related to the behavior of connectivity discussed in Section 3.1: indeed, larger hydraulic conductivity estimates may compensate for the smaller degree of connectivity exhibited by gravel within the SISIM set of realizations.

Model identification/discrimination criteria (for the definitions, see Deliverable 1.4a) have been applied to rank realizations of both generation methods. Table 3.1 collects the values of the diverse criteria evaluated for the realization that, within each set, minimizes KIC. The best realization within the TPROGS set provides better results according to all criteria compared to its counterpart in SISIM.

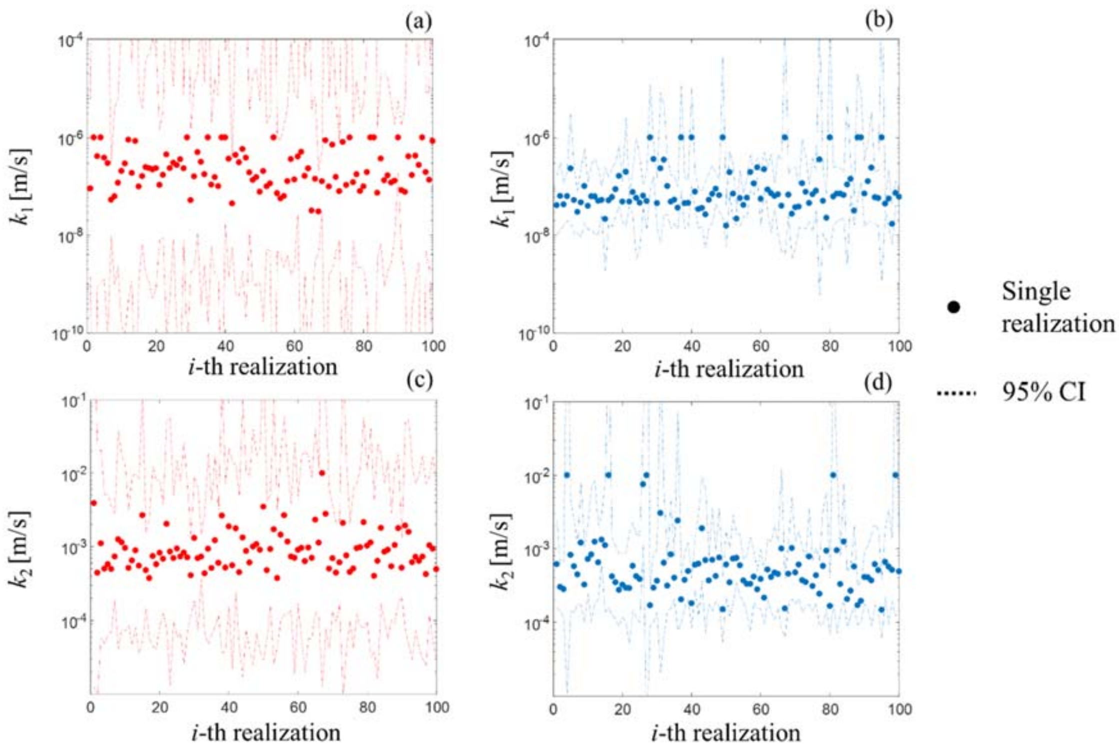

Figure 3.6. Hydraulic conductivity estimates of clay (a-b) and gravel (c-d), obtained for SISIM (a-c) and TPROGS (b-d) sets; 95% CIs are also shown.

Criterion	SISIM set	TPROGS set
J	1280	328
NLL	140	113
KIC	140	118
AIC	144	117
AICc	145	117
BIC	146	119

Table 3.1. Results of model identification criteria for the two realizations minimizing KIC amongst the set of SISIM and TPROGS Monte Carlo simulations.

3.4 Hydraulic head predictions from a multi-model approach

Identification criteria also allow estimating the relative degree of likelihood of a model, M_i, among a set of n available models as (see, e.g., Ye et al., 2004)

$$p\left(M_i \middle| \boldsymbol{h_{OBS}}\right) = \frac{\exp\left(-\frac{1}{2}\left(\mathrm{KIC}_i - \mathrm{KIC}_{\min}\right)\right) p\left(M_i\right)}{\sum_{k=1}^{n}\left[\exp\left(-\frac{1}{2}\left(\mathrm{KIC}_k - \mathrm{KIC}_{\min}\right)\right) p\left(M_k\right)\right]} \tag{3.3}$$

where $p\left(M_i \middle| \boldsymbol{h_{OBS}}\right)$ is the posterior probability (or the posterior weight) of model M_i, $\boldsymbol{h_{OBS}}$ is the vector of available data (i.e., 20 hydraulic head measurements in our case), KIC_i is the KIC criterion computed for M_i, $\mathrm{KIC}_{\min}$ is the minimum value of KIC across all n models, and $p\left(M_i\right)$ is the prior probability of M_i. In our case, since all realizations are equally likely, we set $p\left(M_i\right) = 1/n$.

A multi-model approach (Ye et al., 2004) allows to provide estimates of hydraulic head at the observation wells, $\boldsymbol{h_{EXP}}$, on the basis of (*i*) the hydraulic heads computed in each realization, $\left[\boldsymbol{h} \middle| \boldsymbol{h_{OBS}}, M_k\right]$, and (*ii*) the posterior weights (3.3):

$$\boldsymbol{h_{EXP}} = E\left[\boldsymbol{h} \middle| \boldsymbol{h_{OBS}}, M_k\right] = \sum_{k=1}^{n}\left[\boldsymbol{h} \middle| \boldsymbol{h_{OBS}}, M_k\right] p\left(M_k \middle| \boldsymbol{h_{OBS}}\right) \tag{3.4}$$

The posterior variance associated to $\boldsymbol{h_{EXP}}$ can be computed as

$$Var\left[\boldsymbol{h} \middle| \boldsymbol{h_{OBS}}\right] = \sum_{k=1}^{n}\left(\left[\boldsymbol{h} \middle| \boldsymbol{h_{OBS}}, M_k\right] - \boldsymbol{h_{EXP}}\right)^2 p\left(M_k \middle| \boldsymbol{h_{OBS}}\right). \tag{3.5}$$

Equations 3.4 and 3.5 have been evaluated by setting n =100 and considering SISIM and TPROGS realizations. Values of $\boldsymbol{h_{EXP}}$ versus $\boldsymbol{h_{OBS}}$ are depicted in Figure 3.7. Error bars of amplitude $2\sqrt{Var\left[\boldsymbol{h} \middle| \boldsymbol{h_{OBS}}\right]}$ are also shown. It clearly appears that the best estimates of hydraulic head are those computed from the TPROGS set (Fig.3.7b), which also exhibit lower (posterior) variances compared to their SISIM counterparts (Fig.3.7a).

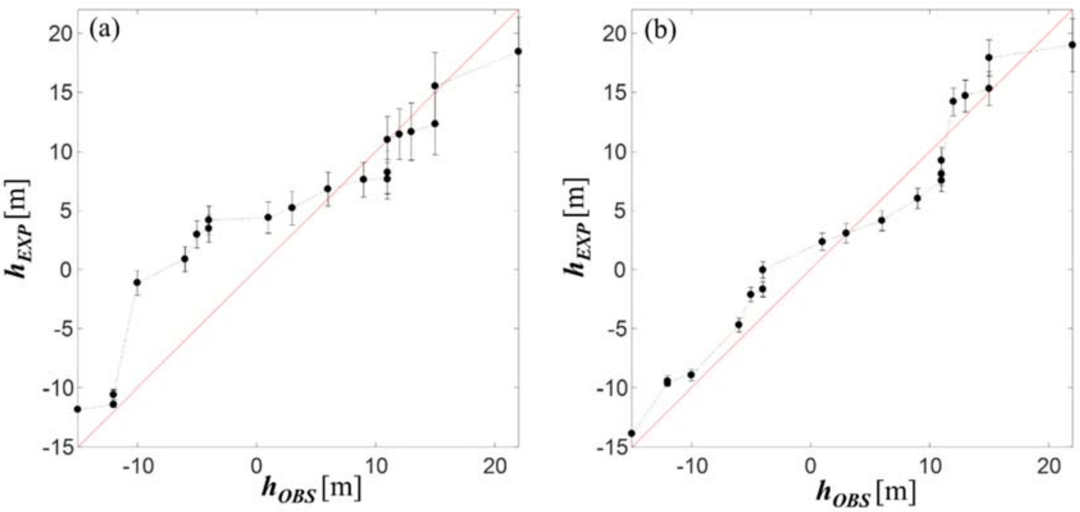

Figure 3.7 Multi-model hydraulic head estimates versus observed hydraulic heads evaluated over the set of (a) SISIM and (b) TPROGS realizations. Error bars are computed as $\boldsymbol{h}_{EXP} \pm \sqrt{Var\left[\boldsymbol{h} \middle| \boldsymbol{h}_{OBS}\right]}$.

References

Carle, S.F., Fogg, G.E. 1996. Transition probability-based indicator geostatistics. Math. Geol. 28, 4, 453-477.

Carle, S. F., Fogg, G.E. 1997. Modelling spatial variability with one and multidimensional continuous-lag Markov chains. Math. Geol. 29, 7, 891-918.

Cvetkovic, V., Fiori, A., Dagan, G. 2014. Solute transport in aquifers of arbitrary variability: A time-domain random walk formulation. Water Resources Research, 50, 5759–5773. https://doi.org/10.1002/2014WR015449.

Dell'Oca, A., Riva, M., Guadagnini, A., 2017. Moment-based metrics for global sensitivity analysis of hydrological systems. Hydrol. Earth Syst. Sci. 21, 6219-6234. https://doi.org/10.5194/hess-21-6219-2017.

Deutsch C.V., Journel A.G. GSLIB, 1992. Geostatistical software library and user's guide. New York, Oxford, Oxford university press. doi:10.1016/0098-3004(94)90041-8.

Doppler, T., Franssen, H.J.H., Kaiser, H.P., Kuhlman, U., Stauffer, F., 2007. Field evidence of a dynamic leakage coefficient for modelling river–aquifer interactions. J. Hydrol. 347, 177-187. https://doi.org/10.1016/j.jhydrol.2007.09.017.

Ghanem, R.G., Spanos, P.D., 1991. Stochastic Finite Elements: A Spectral Approach, Springer, N. Y.

Grimmet, G. 2000. Percolation. Berlin, Springer.

Henri, C. V., Fernandez-Garcia, D., de Barros, F. P. J. 2015. Probabilistic human health risk assessment of degradation-related chemical mixtures in heterogeneous aquifers: Risk statistics, hot spots, and preferential channels. Water Resources Research 51, 4086–4108. https://doi.org/10.1002/2014WR016717.

Hovadik J. M, Larue D. K. 2007. Static characterizations of reservoirs: refining the concepts of connectivity and continuity. Petrol Geosci. 13(3), 195–211.

Kaleris, V., 1998. Quantifying the exchange rate between groundwater and small streams. J. Hydraulic Res. 36 (6), 913-932.

Knudby, C., Carrera, J. 2005. On the relationship between indicators of geostatistical, flow and transport connectivity. Advances in Water Resources 28(4), 405–421. https://doi.org/10.1016/j.advwatres.2004.09.001.

Le Maître, O., Knio, O., 2010. Spectral methods for uncertainty quantification. Scientific Computation, Springer, Heidelberg, Germany. https://doi.org/10.1007/978-90-481-3520-2_1.

Lee S.Y., Carle S.F., Fogg G.E. 2007. Geological heterogeneity and comparison of two geostatistical models: sequential Gaussian and transition probability-based geostatistical simulation. Advances in Water Resources 30, 1914-1932 doi:10.1016/j.advwatres.2007.03.005.

Maione, U., Paoletti, A. and Grezzi, G., 1991. Studio di gestione coordinata delle acque di superficie e di falda nel territorio compreso fra i fiumi Adda e Oglio e delimitato dalle Prealpi e dalla linea settentrionale di affioramento dei fontanili. (Study on surface and subsurface water management in the area between the Adda and Oglio river, the Prealpi line and the springs line).

Morris, M.D., 1991. Factorial sampling plans for preliminary computational experiments. Technometrics 33, 161–174.

Neuman, S. P., Di Federico, V. 2003. Multifaceted nature of hydrogeologic scaling and its interpretation. Reviews of Geophysics 41(3), 1014. https://doi.org/10.1029/2003RG000130.

Neuman, S. P. 2008. Multiscale relationships between fracture length, aperture, density and permeability. Geophysical Research Letters 35(22), L22402. https://doi.org/10.1029/2008GL035622.

Rametta, D., "Interazione tra reticolo idrografico superficiale e acquifero sotterraneo nella modellistica idrologica distribuita (Study on surface-subsurface water interaction by means of a distribute model)", Master Thesis, Politecnico di Milano, Milano (2008).

Renard, P., Allard, D. 2013. Connectivity metrics for subsurface flow and transport. Advances in Water Resources 51, 168–196. https://doi.org/10.1016/j.advwatres.2011.12.001.

Sobol, I.M., 1993. Sensitivity estimates for nonlinear mathematical models. Math. Modeling. Comput. 1, 407–414.

Sobol, I. M., 2001. Global sensitivity indices for nonlinear mathematical models and their Monte Carlo estimates. Math. Comput. Simulat. 55(1–3), 271–280. doi: 0.1016/S0378-4754(00)00270-6.

Stauffer, D. Aharony, A. 1992. Introduction to percolation theory (2nd. Edn). Taylor & Francis, London.

Zinn, B., Harvey, C. F. 2003. When good statistical models of aquifer heterogeneity go bad: A comparison of flow, dispersion, and mass transfer in connected and multivariate Gaussian hydraulic conductivity fields. Water Resources Research 39(3). https://doi.org/10.1029/2001WR001146.

Xiu, D., Karniakidis, G.E., 2002. The Wiener-Askey polynomial chaos for stochastic differential equations. SIAM J. Sci. Comput. 24, 614-644. https://doi.org/10.1137/S1064827501387826.

Ye, M., Neuman, S.P., Meyer, P.D. 2004. Maximum likelihood Bayesian averaging of spatial variability models in unsaturated fractured tuff. Water Resour. Res. 40(5), W05113. doi: 10.1029/2003WR002557.

ANNEX I – List of monitoring wells at Cremona aquifer

X_{GB} (m)	Y_{GB} (m)	Code	City	Hydraulic HEAD (m.a.s.l)
1546246	5058675	PO0160890R0001	CURNO	147.39
1552422	5057977	PO0160240R0296	BERGAMO	179.67
1548663	5057222	PO016123NU0001	LALLIO	152.63
1539673	5055769	PO0162090R1633	SUISIO	187.10
1554164	5053751	559	ZANICA	170.21
1544489	5052062	PO0161530R0004	OSIO SOTTO	134.90
1553315	5049728	PO0162220U0004	URGNANO	101.83
1545606	5049590	40	BOLTIERE	157.72
1548113	5048625	PO0160750U0003	CISERANO	161.54
1548206	5047689	PO0160110U0005	ARCENE	114.58
1550916	5047610	539	SPIRANO	155.77
1544065	5047581	565	PONTIROLO N	63.58
1548706	5047200	386	ARCENE	76.35
1553984	5046280	454	COLOGNO S	71.85
1555440	5046169	456	COLOGNO S	78.90
1545936	5046152	518	PONTIROLO N	66.07
1550487	5045663	PO0161290R0001	LURANO	93.14
1543323	5041854	471	FARA GERA D'ADDA	86.35
1546804	5041457	322	TREVIGLIO	98.44
1546081	5041378	PO016219NUP001	TREVIGLIO	68.92
1544123	5041129	329	TREVIGLIO	63.53
1552699	5040223	80	CARAVAGGIO	70.09
1545540	5040023	324	TREVIGLIO	155.34
1555554	5038707	171	FORNOVO S.G.	104.44
1550740	5037697	78	CARAVAGGIO	106.97
1544537	5036799	439	CASIRATE D'ADDA	111.95
1547168	5036352	64	CALVENZANO	109.48
1548578	5035713	PO0161350U0001	MISANO DI GERA D'ADDA	111.97
1547459	5034881	PO019112NU1123	VAILATE	110.28
1540446	5033610	PO019084NRA002	RIVOLTA D'ADDA	113.58
1554749	5030589	PO019094NU0944	SERGNANO	147.76
1546163	5026783	PO0190660U0002	PALAZZO PIGNANO	106.53
1553178	5025240	PO0190350UA005	CREMA	139.65
1537605	5023199	PO098003NR0063	BOFFALORA D'ADDA	143.26
1552672	5022953	PO019035NRA001	CREMA	115.51
1542996	5021730	PO098025NR0110	CRESPIATICA	138.77
1554037	5020335	PO019081NUP001	RIPALTA CREMASCA	147.67
1543975	5018387	PO098024NR0087	CORTE PALASIO	160.49
1551368	5017127	PO0190340U0001	CREDERA RUBBIANO	149.36

Table A.1. List of monitoring wells at which GSA metrics have been evaluated and used during the calibration procedures (ordered from North to South).

ANNEX II – List of water springs at Cremona aquifer

X_{GB}	Y_{GB}	NAME	CITY	VILLAGE
1540855	5023582	ALIPRANDA	CR	DOVERA
1540855	5023612	ALIPRANDA	CR	DOVERA
1543450	5035830	ARZAGO D'ADDA_1	BG	ARZAGO D'ADDA
1544300	5036350	ARZAGO_2	BG	ARZAGO D'ADDA
1544250	5036580	ARZAGO_3	BG	ARZAGO D'ADDA
1542920	5037130	ARZAGO_4	BG	ARZAGO D'ADDA
1546528	5032237	BALARIN	CR	BVAILATE
1538834	5030738	BALDROLA	CR	RIVOLTA D'ADDA
1549924	5034089	BENZONA	CR	CAPRALBA
1547904	5034058	BETTA'	CR	VAILATE
1546286	5033150	BIANCA(VIGNOLO)	CR	VAILATE
1545357	5034031	BOGINO	CR	VAILATE
1539568	5028467	BONTEMPA	CR	SPINO D'ADDA
1539752	5025488	BORLINA	CR	SPINO D'ADDA
1539524	5030392	BOSCA	CR	RIVOLTA D'ADDA
1545855	5031906	BREDE	CR	TORLINO VIMERCATI
1545800	5031908	BREDE	CR	TORLINO VIMERCATI
1546767	5032436	BURLENGO	CR	VAILATE
1543008	5022996	BUS DA VALENT	CR	DOVERA
1541474	5024847	BUSCHETT	CR	DOVERA
1547190	5032246	CAPRI	CR	TORLINO VIMERCATI
1550770	5034300	CARAVAGGIO_1	BG	CARAVAGGIO
1549950	5036200	CARAVAGGIO_2	BG	CARAVAGGIO
1549160	5036660	CARAVAGGIO_3	BG	CARAVAGGIO
1551800	5036730	CARAVAGGIO_4	BG	CARAVAGGIO
1549670	5037800	CARAVAGGIO_5	BG	CARAVAGGIO
1547150	5032552	CARRERE	CR	VAILATE
1538332	5028022	CASCINETTO DI SPINO	CR	SPINO D'ADDA
1541133	5031298	CAVO DI PANDINO	CR	PANDINO
1539360	5033270	CIOCCHERA	CR	RIVOLTA D'ADDA
1542080	5028984	COLOMBAROLO	CR	PANDINO
1548195	5032404	COLOMBERA	CR	CAPRALBA
1541530	5028191	CURNIN	CR	PANDINO
1544070	5029630	DAL PIR	CR	PANDINO
1547143	5029256	DEI BORNACI	CR	TORLINO VIMERCATI
1546377	5034224	DEI BUCHI	CR	VAILATE
1546906	5033303	DEI GRASSI	CR	VAILATE
1547340	5027750	DEI PENSIONATI	CR	TRESCORE CREMASCO
1546340	5030550	DEL CASINETTO	CR	TORLINO VIMERCATI

1547042	5029656	DEL CIMITERO DI TORLINO	CR	TORLINO VIMERCATI
1548895	5032596	DEL CIMITERO EST	CR	CAPRALBA
1547030	5029240	DEL DEPURATORE	CR	TORLINO VIMERCATI
1539591	5029231	DEL PRETE	CR	PANDINO
1544420	5027280	DEL TORMO DI PANDINO	CR	PANDINO
1550703	5033226	DELE LOTTE	CR	CAPRALBA
1545462	5032218	DELLA CA'	CR	VAILATE
1546745	5030321	DELL'ACQUAROSSA MEZZO	CR	TORLINO VIMERCATI
1546641	5030483	DELL'ACQUAROSSA NORD	CR	TORLINO VIMERCATI
1546820	5030267	DELL'ACQUAROSSA SUD	CR	TORLINO VIMERCATI
1546846	5028928	DELLE BREDE EST	CR	TORLINO VIMERCATI
1550848	5032569	DELLE CANNE	CR	CAPRALBA
1550850	5032607	DELLE CANNE	CR	CAPRALBA
1548357	5034128	DELLE GUARDIE	CR	VAILATE
1547207	5031172	DESGIO'	CR	PIERANICA
1541184	5027249	DI CASA	CR	PANDINO
1550970	5027000	DI CREMOSANO EST	CR	CREMOSANO
1550820	5027040	DI CREMOSANO OVEST	CR	CREMOSANO
1544351	5029293	DI SAS	CR	PANDINO
1546706	5029551	DI TORLINO	CR	TORLINO VIMERCATI
1546787	5029480	DI TORLINO SUD	CR	TORLINO VIMERCATI
1542685	5024312	DOVEROLA	CR	DOVERA
1543467	5022582	DOVEROLO	CR	DOVERA
1541377	5025636	EL RI	CR	DOVERA
1541376	5024600	FALCONA	CR	DOVERA
1539384	5030379	FALCONETTA	CR	RIVOLTA D'ADDA
1549363	5032086	FARINATE	CR	CAPRALBA
1539775	5024317	FASOLA	CR	DOVERA
1546524	5035108	FONTANELLA DEI DOSSI	CR	VAILATE
1538457	5025675	FONTANELLA DI SPINO	CR	SPINO D'ADDA
1547556	5031891	FONTANELLA DI TORLINO	CR	TORLINO VIMERCATI
1545716	5032274	FONTANELLA DI VAILATE	CR	VAILATE
1553969	5033213	FONTANINE	CR	SERGNANO
1549590	5031487	FONTANONE DI CAPRALBA	CR	CAPRALBA
1549620	5031535	FONTANONE DI CAPRALBA	CR	CAPRALBA
1549627	5031671	FONTANONE DI CAPRALBA	CR	CAPRALBA
1540970	5027585	FONTANONE DI PANDINO	CR	PANDINO
1546745	5031173	FONTANONE DI TORLINO	CR	TORLINO VIMERCATI

1552900	5037560	FORNOVO SAN GIOVANNI	BG	FORNOVO SAN GIOVANNI
1541776	5022357	FRACAVALLA	CR	DOVERA
1539555	5031102	FRIZZODI EST	CR	RIVOLTA D'ADDA
1539245	5030817	FRIZZONI DI MEZZO	CR	RIVOLTA D'ADDA
1539178	5031038	FRIZZONI OVEST	CR	RIVOLTA D'ADDA
1542289	5024466	GARATA	CR	DOVERA
1541578	5026616	GRADELLA	CR	PANDINO
1546611	5030071	LA MORTA	CR	TORLINO VIMERCATI
1543565	5022540	LA VAL	CR	DOVERA
1539856	5035128	LAGAZZO	CR	RIVOLTA D'ADDA
1537834	5030579	LAGAZZONE	CR	RIVOLTA D'ADDA
1538134	5028712	LAVANDINO	CR	SPINO D'ADDA
1548282	5031947	MACCHERONE	CR	CAPRALBA
1548347	5031953	MACCHERONE	CR	CAPRALBA
1548412	5031960	MACCHERONE	CR	CAPRALBA
1547678	5022824	MELESA	CR	BAGNOLO CREMASCO
1540000	5031994	MERLO' DI MEZZO	CR	RIVOLTA D'ADDA
1540084	5031891	MERLO' EST	CR	RIVOLTA D'ADDA
1539790	5032140	MERLO OVEST	CR	RIVOLTA D'ADDA
1550039	5034878	MISANO	BG	MISANO DI GERA D'ADDA
1549100	5034100	MISANO DI GERA D'ADDA	BG	MISANO DI GERA D'ADDA
1549530	5035160	MISANO DI GERA D'ADDA_1	BG	MISANO DI GERA D'ADDA
1549930	5035770	MISANO DI GERA D'ADDA_2	BG	MISANO DI GERA D'ADDA
1549200	5035970	MISANO DI GERA D'ADDA_3	BG	MISANO DI GERA D'ADDA
1549950	5036050	MISANO DI GERA D'ADDA_4	BG	MISANO DI GERA D'ADDA
1541599	5030212	MOIA	CR	PANDINO
1546036	5032387	MONIGHET	CR	VAILATE
1552782	5031477	MORGOLA	CR	SERGNANO
1537406	5025402	MOZZANICA	CR	SPINO D'ADDA
1537423	5025438	MOZZANICA	CR	SPINO D'ADDA
1553000	5033480	MOZZANICA	BG	MOZZANICA
1549773	5031017	ORA	CR	CAPRALBA
1548593	5031354	ORIOLA	CR	CAPRALBA
1548583	5031402	ORIOLA	CR	CAPRALBA
1540594	5025945	PIERO FRA	CR	PANDINO
1537456	5025385	PORTICO	CR	SPINO D'ADDA
1548885	5032818	QUARANETINA	CR	CAPRALBA
1548082	5032526	QUARANTA	CR	CAPRALBA
1548889	5032662	QUARANTINA	CR	CAPRALBA
1547465	5029812	REMORTIZZO	CR	PIERANICA

1537600	5028706	RESEGA	CR	SPINO D'ADDA
1539532	5026731	RIOLA	CR	SPINO D'ADDA
1544062	5030521	ROGGETTO	CR	PANDINO
1537673	5027598	ROGGIONE	CR	SPINO D'ADDA
1544947	5029896	SABBIANINO EST	CR	PANDINO
1544790	5029918	SABBIANINO OVEST	CR	PANDINO
1553417	5030465	SCHIAVA	CR	SERGNANO
1553424	5030361	SCHIAVA	CR	SERGNANO
1548332	5031632	SEREDEI	CR	CAPRALBA
1547470	5032472	SIMONETTA	CR	TORLINO VIMERCATI
1542885	5025685	SMERDAROLO	CR	DOVERA
1542835	5025713	SMERDAROLO	CR	DOVERA
1546547	5031651	STAFI'	CR	TORLINO VIMERCATI
1541661	5024966	STELLA	CR	DOVERA
1540456	5027334	TINELLA	CR	PANDINO
1542073	5025720	VALLE DELL'ORTO	CR	DOVERA
1548260	5034255	VALLETTA	CR	VAILATE
1548260	5034255	VALLETTA	CR	VAILATE
1546648	5022108	VALMARZA	CR	BAGNOLO CREMASCO
1537683	5029533	VILLANA	CR	SPINO D'ADDA
1544066	5030176	ZECCA	CR	PANDINO

Table A.2. List of Spring considered in the model (alphabetic order).

ANNEX III – Spring flow rate measurements at Cremona aquifer.

Date	Measurement
01.12.1988	11.75
01.01.1989	8.42
01.04.1989	9.44
01.06.1989	19.02
01.07.1989	23.24
01.08.1989	16.58
01.12.1989	9.39
01.03.1990	5.79
01.04.1990	8.81
01.06.1990	26.53
01.07.1990	18.92
01.09.1990	15.14
01.11.1990	16.96
Mean value	14.62

Table A.3. Discharge measurements (m^3/s) collected during the year 1989-1990. The cumulative value of the 35 sections reported in Figure 2.7 is reported.

day	Misana	Quarantina	Acquarossa upstream	Acquarossa downstrem
	X_{GB} = 1550039; Y_{GB} = 5034878	X_{GB} = 1549362; Y_{GB} = 5032086	X_{GB} = 1546641; Y_{GB}= 5030483	X_{GB} = 1546745; Y_{GB}= 5030321
31.03.09	0.534	0.25	0.296	0.343
06.04.09	0.494	0.173	0.345	0.436
17.04.09	0.391	0.192	0.306	0.378
23.04.09	0.518	0.182		
05.05.09	0.515	0.241		
13.05.09	0.514	0.242		0.252
22.05.09	0.457	0.134		0.139
27.05.09	0.556	0.256		0.295
08.06.09	0.557	0.183		0.304
12.06.09	0.476	0.199		
19.06.09	0.445	0.17	0.245	0.452
03.07.09	0.713	0.195		0.671
14.07.09	0.618	0.174	0.137	0.352
29.07.09	0.659	0.14	0.223	0.505
02.09.09	0.627	0.498		0.686
Mean value	0.52	0.20	0.27	0.36

Table A.4. Discharge measurements (m^3/s) collected during the year 2009.